

# Elliptical galaxies with rapidly decreasing velocity dispersion profiles: NMAGIC models and dark halo parameter estimates for NGC 4494

Lucia Morganti<sup>1\*</sup>, Ortwin Gerhard<sup>1†</sup>, Lodovico Coccato<sup>2</sup>, Inma Martinez-Valpuesta<sup>1</sup>,  
Magda Arnaboldi<sup>2,3</sup>

<sup>1</sup> *Max-Planck-Institut für extraterrestrische Physik, Postfach 1312, Giessenbachstr., D-85741 Garching, Germany*

<sup>2</sup> *European Southern Observatory, Karl-Schwarzschild-Strae 2, D-85748 Garching, Germany*

<sup>3</sup> *INAF, Osservatorio Astronomico di Pino Torinese, I-10025 Pino Torinese, Italy*

MNRAS accepted.

## ABSTRACT

NGC 4494 is one of several intermediate-luminosity elliptical galaxies inferred to have an unusually diffuse dark matter halo. We use the  $\chi^2$ -made-to-measure particle code NMAGIC to construct axisymmetric models of NGC 4494 from photometric and various kinematic data. The extended kinematics include light spectra in multiple slitlets out to  $3.5R_e$ , and hundreds of planetary nebulae velocities out to  $\simeq 7R_e$ , thus allowing us to probe the dark matter content and orbital structure in the halo.

We use Monte Carlo simulations to estimate confidence boundaries for the halo parameters, given our data and modelling set-up. We find that the true potential of the dark matter halo is recovered within  $\Delta G(\text{merit function}) \lesssim 26$  ( $\Delta\chi^2 \lesssim 59$ ) at 70% confidence level (C.L.), and within  $\Delta G \lesssim 32$  ( $\Delta\chi^2 \lesssim 70$ ) at 90% C.L.. These numbers are much larger than the usually assumed  $\Delta\chi^2 = 2.3(4.6)$  for 70% (90%) C.L. for two free parameters, perhaps case-dependent, but calling into question the general validity of the standard assumptions used for halo and black hole mass determinations.

The best-fitting models for NGC 4494 have a dark matter fraction of about  $0.6 \pm 0.1$  at  $5R_e$  (70% C.L.), and are embedded in a dark matter halo with circular velocity  $\sim 200 \text{ km s}^{-1}$ . The total circular velocity curve (CVC) is approximately flat at  $v_c = 220 \text{ km s}^{-1}$  outside  $\sim 0.5R_e$ . The orbital anisotropy of the stars is moderately radial. These results are independent of the assumed inclination of the galaxy, and edge-on models are preferred. Comparing with the halos of NGC 3379 and NGC 4697, whose velocity dispersion profiles also decrease rapidly from the center outwards, the outer CVCs and dark matter halos are quite similar. NGC 4494 shows a particularly high dark matter fraction inside  $\sim 3R_e$ , and a strong concentration of baryons in the center.

**Key words:** galaxies: kinematics and dynamics – galaxies: elliptical and lenticular, cD – galaxies: individual: NGC 4494 – galaxies: halos – cosmology: dark matter – methods: N-body simulations

## 1 INTRODUCTION

The formation and evolution of elliptical galaxies has been an important issue in extragalactic astrophysics since a long time. Being collisionless to a very good approximation, ellipticals retain relics of their formation history in the present-day orbital structure, especially in their halos due to the

longer dynamical time scales. According to the currently favoured hierarchical formation scenario in a  $\Lambda$ CDM cosmology, these halos are dark matter dominated. The ambitious task of inferring both the orbital structure and mass distribution of ellipticals is commonly tackled by dynamical modelling of the observational data.

Unfortunately, the lack of an ubiquitous tracer such as HI gas in spiral galaxies (but see Bertola et al. 1993; Franx et al. 1994; Oosterloo et al. 2002) makes mass measurements in elliptical galaxies challenging. The strongest

\* E-mail: morganti@mpe.mpg.de

† E-mail: gerhard@mpe.mpg.de

evidence for dark matter halos is found for giant ellipticals whose mass distribution can be determined from X-ray emission of the hot gas (*e.g.* Loewenstein & White 1999; Humphrey et al. 2006; Das et al. 2010a) or strong gravitational lensing techniques (*e.g.* Maoz & Rix 1993; Keeton 2001; Treu & Koopmans 2004; Auger et al. 2010). These studies are consistent with massive dark halos, and nearly isothermal total mass profiles (Ciotti et al. 2009).

By contrast, the situation with less massive, X-ray faint ellipticals is more controversial. However, dynamical models, particularly when fitting higher order moments of the line-of-sight velocity distribution (LOSVD) from stellar absorption lines, eventually ascertained the presence of dark matter halos around these intermediate-luminosity ellipticals and are generally consistent with flat circular velocity curves. With LOSVD measurements limited by the rapid fall-off of the stellar surface brightness, the kinematics of discrete tracers such as planetary nebulae (PNe) and globular clusters (GCs) usually represent the only possibility to probe the mass distribution and orbital structure beyond  $2R_e$ , in the realm of dark matter (*e.g.* Hui et al. 1995; Méndez et al. 2001; Douglas et al. 2002; Peng et al. 2004; de Lorenzi et al. 2008, 2009; Napolitano et al. 2009; Das et al. 2011; Napolitano et al. 2011; Deason et al. 2012).

Curiously, the PNe velocity dispersion profiles of some of the nearby intermediate-luminosity ellipticals show a strong, quasi-Keplerian decline with radius outside  $1R_e$  (Coccato et al. 2009), suggesting very little (if any) dark matter (Romanowsky et al. 2003). The aim of the present paper is to expand the sample of modelled quasi-Keplerian intermediate luminosity ellipticals, focussing on NGC 4494, and then compare the results with those previously obtained for other galaxies of this class, namely NGC 4697 (de Lorenzi et al. 2008, hereafter DL08) and NGC 3379 (de Lorenzi et al. 2009, hereafter DL09).

NGC 4494 is an E1-E2 elliptical galaxy in the outer regions of the Virgo cluster, with a smooth light profile and an intermediate stellar mass of about  $10^{11} M_\odot$  (Foster et al. 2011, hereafter F11). It has been variously described as a loose group member (Forbes et al. 1996) or isolated galaxy (Lackner & Ostriker 2010). NGC 4494 is classified as a fast rotator by Emsellem et al. (2011,  $\lambda_R \simeq 0.2$ ). Among the peculiarities of this galaxy, a sharp central ring of dust (Forbes et al. 1995; Lauer et al. 2005), a kinematically decoupled core (Bender et al. 1994; Krajnović et al. 2011), moderate rotation  $\sim 60 \text{ km s}^{-1}$  out to  $\sim 3R_e$  (Proctor et al. 2009), and an outward-decreasing  $\lambda_R$ -profile (Coccato et al. 2009) have been reported. The velocity dispersion profile of NGC 4494 decreases rapidly from about  $160 \text{ km s}^{-1}$  in the center to about  $70 \text{ km s}^{-1}$  at  $\sim 7R_e$  (Napolitano et al. 2009, hereafter N09), hinting to a possible deficiency in dark matter. Also, the X-ray flux of NGC 4494 is two hundred times fainter than that of other galaxies of the same optical luminosity, which has been interpreted as the result of a recent interaction which depleted the gas, or again as evidence for little dark matter (O’Sullivan & Ponman 2004; Fukazawa et al. 2006).

NGC 4494 has been recently modelled using spherical Jeans models (N09), and axisymmetric particle models constructed with the iterative method (Rodionov & Athanassoula 2011). The available observational data, which included PNe velocities out to  $\sim 7R_e$

(N09), were best fit by low concentration dark halos, with some uncertainties related to the adopted modelling assumptions, the differences between the fits for different models (N09), and the limited number of explored models (Rodionov & Athanassoula 2011).

Recently, new observational data consisting of stellar absorption line kinematics in multiple slitlets out to  $\sim 3.5R_e$  became available for this galaxy (Proctor et al. 2009, F11). Moreover, in the work of Deason et al. (2012) NGC 4494 appeared as an outlier with curiously low dark matter fraction within  $5R_e$ , with respect to model predictions assuming either a Salpeter or a Chabrier initial mass function. These facts prompted us to undertake a further careful analysis of the dark matter content and orbital structure of NGC 4494, incorporating as many observational data as currently available and assessing the uncertainties in the recovery of dark halo parameters via dynamical models.

In this paper, we construct new dynamical models fitting all available photometric and kinematic data with the flexible particle code NMAGIC (de Lorenzi et al. 2007, hereafter DL07), which implements a modified version of the made-to-measure (M2M) technique proposed by Syer & Tremaine (1996), suitable for the modelling of observational data with errors ( $\chi^2$ M2M). NMAGIC works by slowly correcting the particle weights of an evolving N-body system until a satisfactory compromise is achieved between the goodness-of-fit to the observational data, and some degree of regularization of the underlying particle model. More recent implementations of the method can be found in Dehnen (2009), who proposed a different technique for the weight adaptation, Long & Mao (2010), and Morganti & Gerhard (2012, hereafter MG12), who introduced a Moving Prior Regularization method to generate smooth  $\chi^2$ M2M particle models fitting noisy data without erasing the global phase-space structures.

So far, the M2M technique has been used to investigate the dynamics of the Milky Way’s bulge and disk (Bissantz et al. 2004; Long et al. 2013), the mass distribution and orbital structure in the outer halos of elliptical galaxies (DL08; DL09; Das et al. 2011), and the dynamics of a sample of SAURON elliptical and lenticular galaxies (Long & Mao 2012). In this paper, we construct axisymmetric NMAGIC models for NGC 4494 which include PNe (N09) and new stellar absorption line kinematics in slitlets (F11), for different dark matter contributions to the total gravitational potential, and for different inclinations.

One of the key points in this work is to study the accuracy with which the parameters of our models can be estimated given the observational data at hand. M2M particle methods work by adjusting the weights of a large number of particles in order to achieve a good match to the data. Similarly, in the more common Schwarzschild methods a large number of orbital weights is adjusted to fit the data. Typically, there are many more weights than data constraints, hence the number of degrees of freedom<sup>1</sup> is likely to be much smaller than the number of data points (Cretton et al. 2000;

<sup>1</sup> The number of degrees of freedom is defined as the number of constraints (data points plus constraints introduced by *e.g.* regularization) minus the number of free parameters (model parameters plus fitted weights).

Gebhardt et al. 2000). However, to determine the effective number of free parameters involved in the modelling is very difficult.

It is common practise to use the relative differences  $\Delta\chi^2 = \chi^2 - \chi_{min}^2$  to measure confidence limits for the subset of parameters specifying the mass model. On the assumption that the observational errors are Gaussian distributed (but see van der Marel et al. 2000), that the model is linear in the parameters, and the number of degrees of freedom is positive,  $\Delta\chi^2$  follows  $\chi^2$ -statistics (*e.g.* Press et al. 1992). Many dynamical modelling studies have therefore estimated, *e.g.*, 68% confidence limits for 1 (2,3) free model parameter(s) from  $\Delta\chi^2 = 1(2.3, 3.5)$  contours in these parameters (*e.g.* van der Marel et al. 1998; Cretton & van den Bosch 1999; Barth et al. 2001; Verolme et al. 2002; Cappellari et al. 2002; Gebhardt et al. 2003; Valluri et al. 2004; Shapiro et al. 2006; Chanamé et al. 2008; Cappellari et al. 2009; van den Bosch & de Zeeuw 2010; Murphy et al. 2011; Adams et al. 2012), but see van den Bosch & van de Ven (2009). Here, prompted by large  $\Delta\chi^2$  values between quite similar models, we use a Monte Carlo simulation approach to estimate confidence intervals for the parameters based on models of NGC 4494-like mock galaxies (see also Press et al. 1992; Gerhard et al. 1998; Thomas et al. 2005).

The paper is organized as follows. In Section 2 we describe the observational data used for NGC 4494. In Section 3 we outline the modelling technique. In Section 4 we construct NGC 4494-like target galaxies and their observables in different dark matter halos, and use them to calibrate the optimal amount of regularization, and to estimate the confidence levels for parameter estimation with our NMAGIC models. Dynamical models of NGC 4494 for a range of dark matter halo potentials and inclinations are then constructed in Section 5. The main implications of our findings are discussed in Section 6. Finally, the paper closes with our conclusions in Section 7.

## 2 OBSERVATIONAL DATA

In this Section we describe the observational data that we will use for modelling the elliptical galaxy NGC 4494. We adopt a distance of 15.8 Mpc (Tonry et al. 2001), so that 1 kpc=13'', a systemic velocity  $v = 1344 \text{ km s}^{-1}$ , from NED, and  $R_e = 49'' \approx 3.77 \text{ kpc}$  (de Vaucouleurs et al. 1991).

### 2.1 Photometric data and deprojection

As photometric data, we use the V-band surface-brightness profile, ellipticity and shape parameter  $a_4$  values of N09. The photometric data extend to  $273''$  along the major axis, and are a combination of *HST* data in the V and I bands inside  $4.3''$  (Lauer et al. 2005), ground-based observations in BVI out to  $32''$  (Goudfrooij et al. 1994), and Megacam data from the Sloan Digital Sky Survey  $g'$  filter (N09). The total extinction-corrected luminosity in the V-band is  $2.6 \times 10^{10} L_{V,\odot}$  (N09).

A Sérsic fit to the surface brightness profile outside the central dust region ( $R > 5.6''$ ) gives  $n = 3.30$  (N09). The observed ellipticity is  $\epsilon = 0.15 - 0.20$  (axis ratio  $q = 0.85 - 0.80$ ) for  $R < R_e/2$ , outside of which NGC 4494 becomes

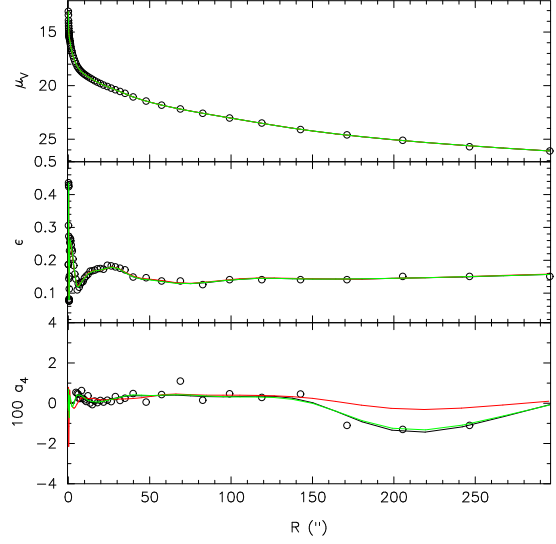


**Figure 1.** From top to bottom: V-band surface-brightness, ellipticity, and fourth-order isophotal shape coefficient  $a_4$  as a function of major-axis projected radius for NGC 4494. Circles are the measurements, lines represent the reprojected values from axisymmetric deprojections obtained with an assumed inclination of  $90^\circ$  (black),  $70^\circ$  (green), and  $45^\circ$  (red).

rounder, with  $\epsilon = 0.13 - 0.15$  ( $q = 0.87 - 0.85$ ) for  $1 - 1.5R_e$ . The radial profiles of surface-brightness, ellipticity, and shape parameter  $a_4$  are shown in Fig. 1.

In our NMAGIC models for the galaxy NGC 4494, we will not use the 2D surface brightness, but rather its 3D deprojected luminosity density. The deprojection of the surface brightness is unique only for spherical or edge-on axisymmetric systems (*e.g.* Gerhard & Binney 1996). Here, we consider axisymmetric deprojections for inclinations  $i = 90^\circ, 70^\circ$ , and  $45^\circ$ , which is very close to the minimum inclination allowed by the observed flattening of NGC 4494 (N09; F11). For each inclination angle, we use the maximum penalized likelihood scheme and program described in Magorrian (1999) to find a smooth axisymmetric density distribution consistent with the surface-brightness profile. The method favours a power-law density profile in the radial region not constrained by photometric data.

The overall good agreement between the measured and reprojected surface-brightness, ellipticity, and shape parameter  $a_4$  is shown in Fig. 1. For  $i = 45^\circ$ , the method apparently has some difficulties in reproducing the boxy isophotes at  $R \sim 200''$  accurately.

### 2.2 Kinematic data

We combine three kinematic data sets in order to achieve the widest possible spatial coverage and probe the mass distribution and orbital structure far out in the halo of NGC 4494. In particular, we use long-slit absorption line kinematics extending out to  $\sim 2R_e$  (Coccato et al. 2009), absorption line kinematics in slitlets out to  $\sim 3.5R_e$  (F11), and PNe line-of-sight velocities reaching  $\sim 7R_e$  (N09). The spatial coverage of the combined kinematic constraints can be appreciated in Fig. 2.

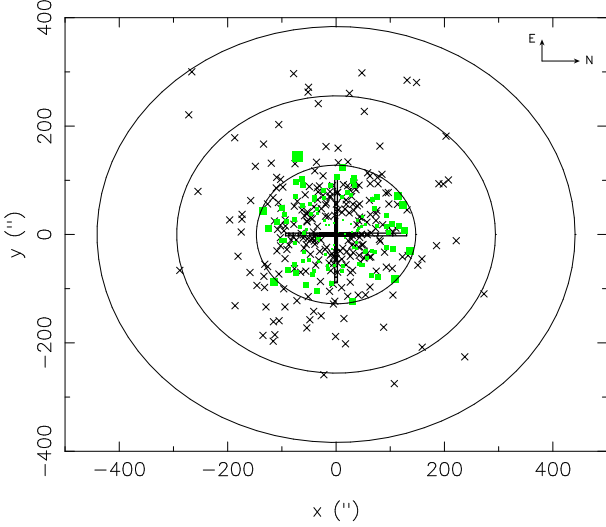


**Figure 2.** Spatial distribution of published kinematic data for NGC 4494. Long-slits along the major and minor axis are plotted, where the  $x$ -axis coincides with the major axis of the galaxy. The positions of PNe are marked by *black crosses*, those of the slitlets by *green squares*. *Ellipses* represent 3, 6, and  $9R_e$ , for an axis ratio  $q = 0.87$ .

### 2.2.1 Stellar-absorption line slit data

Long-slit absorption line kinematics within  $\sim 2R_e$  were presented in Coccato et al. (2009), and consist of line-of-sight velocity  $v$ , velocity dispersion  $\sigma$ , and higher-order Gauss-Hermite coefficients  $h_3$  and  $h_4$ , along the major and minor axis of NGC 4494.

The original data are shown in Fig. 3 with black dots. They are consistent with small or zero rotation along the minor axis, and substantial major axis rotation, flattening beyond  $20''$  at  $V \sim 60 \text{ km s}^{-1}$  out to  $120''$ . In the inner  $10''$  along the major axis, the signature of the decoupled core is apparent. The velocity dispersion decreases from about  $160 \text{ km s}^{-1}$  at the center to about  $80 \text{ km s}^{-1}$  at  $\sim 100''$ .

We noticed a systematic offset between the velocities and  $h_3$  coefficients measured along the major and minor axes in the central arcsec. This leads us to suspect an offset of the minor axis slit from the galaxy centre, in the South direction. The required offset (less than  $1''$ ) is smaller than the slit width and the average seeing. Furthermore, the  $h_3$  measurements along the minor axis are overall negative on both sides, which is unexpected even for a triaxial system with minor axis rotation. For the modelling, we therefore replace the measurements of  $v$  and  $h_3$  along the minor axis with Gaussian random variates with zero mean and  $1\sigma$  dispersion equal to the observational errors.

Inside  $32''$  there are many nearby data points whose respective rms deviations are larger than their error bars. In order to reduce their impact on the modelling, we run a central moving average over the data within  $32''$ , averaging over 7 data points (3 points on each side), and substituting each point with the value of the average. Because the errors of the neighbouring points are very similar, we decided to leave them at their original values.

Then, we minimize the impact of the feature at  $\sim 20''$  along the major axis, which is due to contamination from a

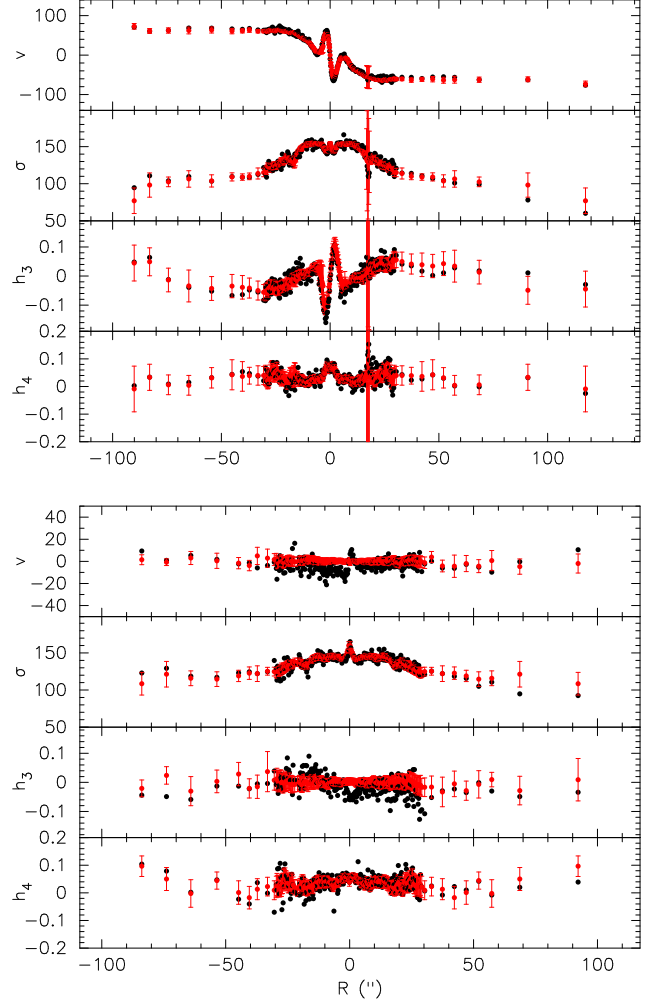


**Figure 3.** Long-slit kinematics along the major (*top*) and minor axis (*bottom*) of NGC 4494. *Black and red dots* represent the original data and the data used for the modelling, respectively. See Section 2.2.1 for details.

foreground star, by artificially increasing the error bars of those measurements.

As we are interested in axisymmetric models of the data, we finally symmetrize the slit data set, as in DL09. In practice, we average the values of the measured kinematics at two similar radii ( $R_+$ ,  $R_-$ ) on both sides of the slit with respect to the center. Since the kinematic data show major axis rotation, we take into account the sign reversal of  $v$  and  $h_3$  when symmetrizing the major axis slit data. Then, the new symmetrized data point is set equal to the weighted mean of the points on both sides, with weights proportional to the inverse square of the original errors. If  $\sigma_+$  and  $\sigma_-$  are the errors on both sides, the new error  $\sigma$  on the symmetrized data points is set equal to the maximum of

$$\frac{2}{\sigma^2} = \frac{1}{\sigma_+^2} + \frac{1}{\sigma_-^2} \quad (1)$$

and half of the deviation between the original data points, which includes systematic errors between both sides of the galaxy.

The resulting data, with their respective error bars, are

shown with red dots in Fig. 3, where they can be compared with the original measurements.

### 2.2.2 Stellar-absorption line slitlets data

We include in our kinematic constraints the measurements of  $v$ ,  $\sigma$ ,  $h_3$ , and  $h_4$  in 115 galaxy light spectra in slitlets recently published by F11, which extend out to  $3.5R_e$ .

F11 discussed the generally good agreement between these data and the long-slit absorption line kinematics of Coccato et al. (2009). Also, they reported that their uncertainties are likely to be slightly underestimated.

On the whole, the absorption line kinematic data do not show significant evidence for minor axis rotation. Therefore, being interested in axisymmetric models of the data, we 4-fold the original sample of slitlets in order to decrease the impact of data asymmetries in our models. To this end we reflect the measurement points around both the galaxy's major and minor axes, maintaining errors, and taking into account the sign reversal of  $v$  and  $h_3$ .

Finally, we look for possible outliers in the 4-folded data set consisting of 460 data points. To this aim, we use the following procedure: for each slitlet, we compute the value of the average field of  $v$ ,  $\sigma$ ,  $h_3$ , and  $h_4$  from its 20 nearest neighbours, excluding the slitlet itself. This average is worked out by excluding the lowest and highest 2 values in the neighbourhood, i.e. considering only the central 80% of the distribution. Moreover, the average is a weighted one, with weights equal to the inverse square of the larger of the individual observational error and the median of the observational errors in the central 80% of the distribution. In the same way, we calculate a weighted rms  $\sigma$  in each neighbourhood. Then, we flag as outlier any point deviating by more than  $2\sigma$  from the weighted mean of its neighbours.

With this procedure, 158 data points are flagged as outliers in velocity and/or velocity dispersion, and removed from the 4-folded data set. Of the resulting data set consisting of 302 slitlets, 68 points are marked as outliers in  $h_3$  or  $h_4$ , and therefore we only consider their velocity and velocity dispersion in the modelling below.

The slitlets data points, together with the outliers determined in this way, are shown in Fig. 4.

### 2.2.3 Planetary nebulae velocities

Our kinematic observables are completed by the 267 PNe line-of-sight velocities obtained by N09 with the Planetary Nebulae Spectrograph (PNS, Douglas et al. 2002). As illustrated in Fig. 2, PNe extend out to  $\sim 7R_e$ .

Fig. 4 shows the comparison of all kinematic data. In the region of overlap, the kinematics of PNe are consistent with those of the stars (see N09, Fig. 6 therein).

In order to look for possible outliers in the sample of PNe, we use the friendless algorithm presented in Merrett et al. (2003), which flags as outlier any object deviating by more than  $n \times \sigma$  from the velocity distribution of its  $M$  nearest neighbours, where  $\sigma$  is the rms computed in each neighbourhood. Adopting  $n = 2.5$  and  $M = 20$ , we remove 10 outliers from the original sample of PNe. These outliers are highlighted in Fig. 5, which shows the projected phase-space distribution of PNe.

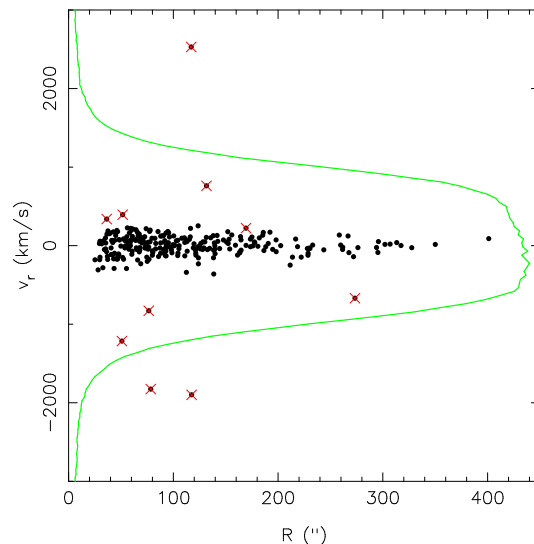


**Figure 5.** Distribution of the line-of-sight velocities of PNe as a function of projected radius. *Red crosses* mark the outliers identified by the friendless algorithm. The PNS filter band-pass is overplotted in *green*.

We are left with a catalogue of 257 PNe, whose size we double by applying point-symmetry, i.e. generating for every PN  $(x, y, v)$  the symmetric PN  $(-x, -y, -v)$ . Such point-symmetric velocity fields are expected in axisymmetric (or triaxial) potentials. From previous experiments we know that increasing the number of PNe by a further factor of two does not improve the modelling significantly.

## 3 MODELLING DATA WITH NMAGIC

In this Section we briefly describe the NMAGIC made-to-measure (M2M) modelling technique. We also explain how the initial particle model is set up, and how the photometric and kinematic target observables are preprocessed for the dynamical modelling.

### 3.1 NMAGIC

The parallel code NMAGIC (DL07) is an implementation of a particle-based method to create  $\chi^2$ M2M models in agreement with observations of galaxies. The algorithm is a slight modification of the technique proposed by Syer & Tremaine (1996), designed to model observational data with errors.

The basic idea behind M2M particle methods is to train a system of  $i = 1, \dots, N$  particles to reproduce the observables of a target galaxy by maximizing the function

$$F = -\frac{1}{2}\chi^2 + \mu S + \mathcal{L} \quad (2)$$

with respect to the particle weights  $w_i$ . This maximization strikes a compromise between the goodness of the fit ( $\chi^2$ ) in terms of deviations between target and particle model observables, and a pseudo-entropy functional

$$S = -\sum_{i=1}^N w_i \left[ \log \left( \frac{w_i}{\bar{w}} \right) - 1 \right] \quad (3)$$

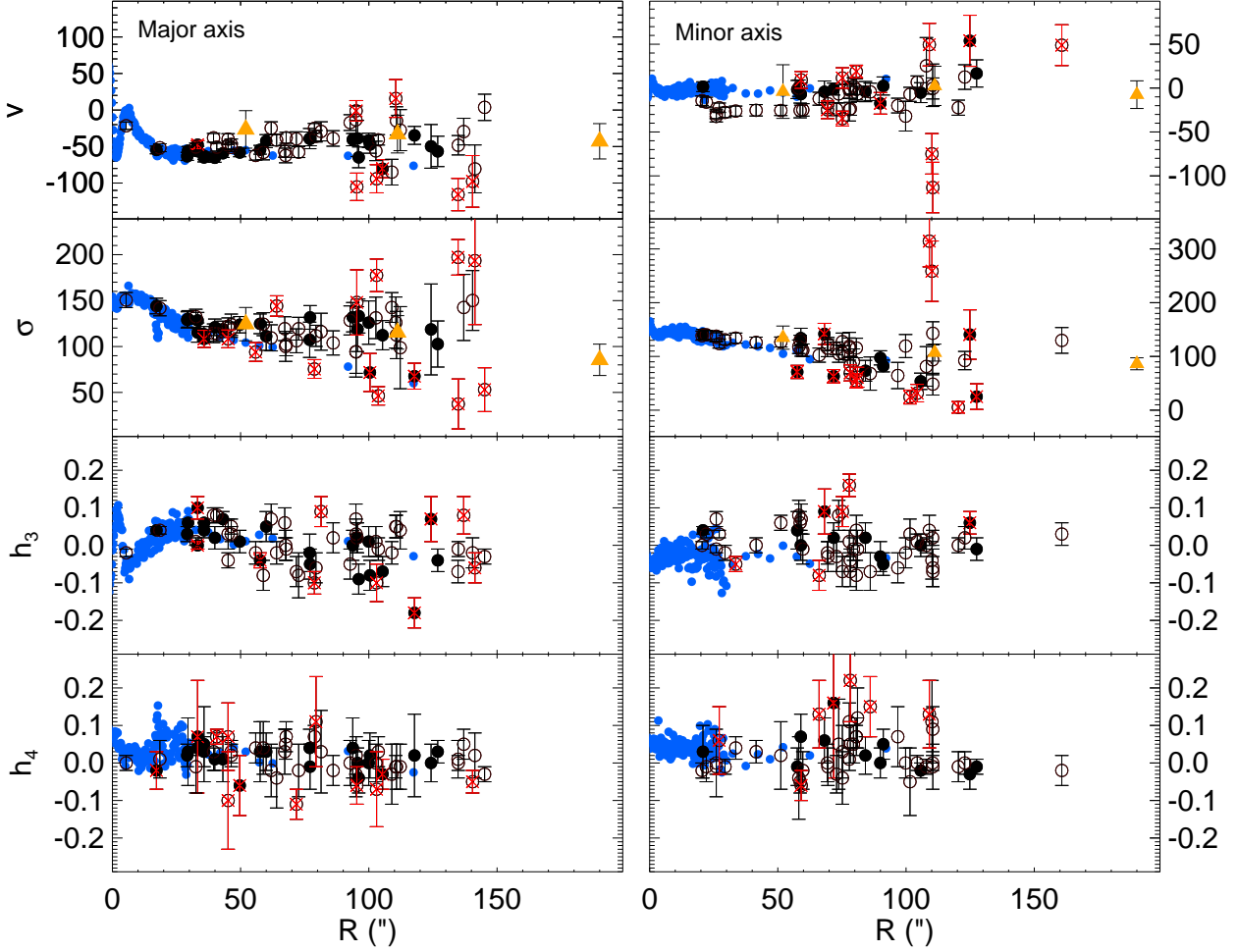


**Figure 4.** Slitlets kinematics in the 4-folded data set (*circles*), compared with long-slit (*blue dots*) and PNe data (*orange triangles*). Left and right column are for the measurements around the major and minor axis, respectively. *Filled circles* represent the data in a cone of  $\pm 15^\circ$  around the axis, while *empty circles* are the data points in cones  $30^\circ \pm 15^\circ$ ,  $60^\circ \pm 15^\circ$ , respectively. Outliers determined by the method described in Section 2.2.2 are marked *red*.

(MG12) which serves the purpose of regularization. Finally, the likelihood term  $\mathcal{L}$  is added to equation (2) to account for the likelihood of a sample of PNe velocities (see DL08).

Since in typical applications the number of particles is much higher than the number of data constraints on the particle model, regularization is essential. In standard M2M, regularization is achieved by pushing the individual particle weights towards a smooth distribution of predetermined priors  $\tilde{w}_i$ , which mirror the initial particle weight distribution and are kept constant during the modelling. As we showed in MG12, such a Global Weight Entropy scheme makes it hard to reconcile smoothness and orbital anisotropies in the final particle model. Therefore, in this work we adopt the alternative Moving Prior Regularization (MPR) method proposed in MG12, and we determine priors which follow the smooth phase-space structures traced by the weight distribution, as the latter adapts to match the observational data. This method facilitates recovering both a smoother and more accurate mass distribution function from noisy data, smoothing over local fluctuations without erasing global phase-space gradients.

Maximizing the function (2) translates into a prescription, the so-called “force-of-change” equation, for correcting the weights of the particles while these are evolved in the total gravitational potential. In generic form this is

$$\frac{dw_i(t)}{dt} = -\varepsilon w_i(t) \left[ \sum_{\text{id}} \xi_{\text{id}} \sum_{j=1}^{J_{\text{id}}} \frac{K_j^{\text{id}}[\mathbf{z}_i(t)]}{\sigma_j^{\text{id}}} \tilde{\Delta}_j^{\text{id}}(t) - \mu \frac{\partial S}{\partial w_i} - \xi_{\text{PN}} \frac{\partial}{\partial w_i} \sum_{j=1}^{J_{\text{PN}}} \ln \mathcal{L}_j \right]. \quad (4)$$

The first term on the right is the  $\chi^2$  derivative term as in DL07, summed over the observational constraints for the different types of data observables, id:  $A_{\text{lm}}$ , slits, and slitlets;  $J_{\text{id}}$  are the respective number of constraints.  $\tilde{\Delta}_j^{\text{id}}$  and  $\sigma_j^{\text{id}}$  are the temporally-smoothed relative deviation and error in observable (id,  $j$ ), and  $K_j^{\text{id}}$  the corresponding kernel evaluated at phase-space position  $\mathbf{z}_i(t)$  of particle  $i$ . The last term has been written as sum over the log likelihoods as in DL08. The notation is explained further in these papers. We have included here additional separate weight factors  $\xi_{\text{id}}$

for the different observables, which we use to optimize the influence of the data on the evolution of the model (see also Long & Mao 2010).

### 3.2 The gravitational potential

The particle modelling technique allows for using both a fixed potential, known a priori, and a time-varying potential, self-consistently computed from the particle distribution. In our dynamical models, we assume that the total gravitational potential is generated by the luminous and dark matter distributions, i.e.

$$\phi = \phi_{\star} + \phi_D. \quad (5)$$

Following Sellwood (2003) and DL07,  $\phi_{\star}$  is frequently computed from the  $N$ -particle model for the light distribution via a spherical harmonic decomposition, assuming a constant mass-to-light ratio  $\Upsilon$ . The value of  $\Upsilon$  is not a fixed parameter, but rather it is determined during the NMAGIC run, simultaneously with the modelling of the observational data (see DL08).

Instead, the dark matter halo potential  $\phi_D$  is parametrized, and has the logarithmic form

$$\phi_D(R, z) = \frac{v_0^2}{2} \ln(r_0^2 + R^2) \quad (6)$$

(Binney & Tremaine 2008), where  $v_0$  and  $r_0$  are a characteristic (constant) circular velocity and scale-length. This mass model has been widely and successfully used to fit galaxies (e.g. Fall & Efstathiou 1980; Persic et al. 1996; Kronawitter et al. 2000; Thomas et al. 2007b, DL09).

Our dynamical models will explore a range of circular velocity curves, whose behaviour at large radii varies between the near-Keplerian decline (when stars dominate the total potential), and a nearly flat (quasi-isothermal) shape obtained for massive dark halos, as shown in Fig. 6.

### 3.3 The initial particle model

We set up initial models of  $N = 750000$  particles extending to  $30R_e$ , i.e.  $\sim 110$  kpc at the distance of NGC 4494.

The density of these initial particle models is given by a spherical deprojection of the circularly-averaged surface brightness profile. We follow the method described in Gerhard (1991) to obtain an isotropic stellar velocity distribution in the total gravitational potential generated by the stars plus the different dark matter halos described above.

The particles' coordinates and velocities are drawn according to the complete distribution function applying the method of Debattista & Sellwood (2000), and particle weights are set equal to  $1/N$ .

Finally, following Kalnajs (1977) and DL08, we switch the sign of the velocity of a fraction of the retrograde particles, with probability

$$p(L_z) = p_0 \frac{L_z^2}{L_z^2 + L_0^2} \quad (7)$$

(where  $p_0 = 0.3$ ,  $L_0 = 0.02$ ), to introduce some angular momentum about the  $z$ -axis, while maintaining a smooth DF in equilibrium. This expedient makes it easier to reproduce the rotation velocity seen in the kinematic data.

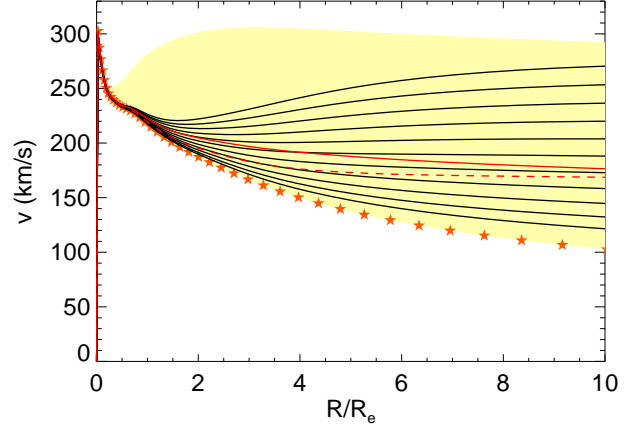


**Figure 6.** The shaded area shows the range of circular velocity curves corresponding to the total gravitational potentials used in the dynamical models. Stars represent the self-consistent case with constant  $M/L$ ; solid lines correspond to models embedded in various spherical dark matter halos. Black lines correspond to dark halos with  $r_0 = 4R_e$  and  $v_0 = [70, \dots, 270]$   $\text{kms}^{-1}$  (from bottom to top). Solid and dashed red lines correspond to  $v_0 = 150 \text{ km/s}$ , and  $r_0 = 3R_e$  and  $5R_e$ , respectively.

### 3.4 Photometric and kinematic observables for the modelling

We now explain how the different photometric and kinematic observational data are processed in order to be used as constraints for the NMAGIC models.

For the photometric observables, the 3D luminosity density profile obtained from the deprojection of the surface-brightness is expanded in spherical harmonic functions, and the expansion coefficients  $A_{lm}$  are used as luminosity constraints (see DL07). These  $A_{lm}$  are computed on a grid of 50 quasi-logarithmically spaced radial shells between  $r_{\min} = 0.01''$  and  $r_{\max} = 20R_e$ , and all terms that would allow non-axisymmetry are set to zero. Poissonian errors are used for the mass in shells, whereas the errors for the higher-order mass moments are determined via Monte Carlo simulations of the density field of the target galaxy (see DL07).

For the long-slits and slitlets data, we use luminosity-weighted kinematic observables. Hence, we add to the target observables the luminosity in each slit cell or slitlet, obtained by integrating the surface brightness distribution with a Monte Carlo algorithm. For the slits, we assume that the slitwidth equals  $5''$ ; for the slitlets, we set the slitwidth equal to the larger value between  $1''$  and the diameter of a circle containing at least 250 particles of the initial particle model, so as to limit particle noise when computing model observables. These slit cell luminosities are independently fitted, with errors set to 1% of the luminosity in each cell.

PNe data are modelled by maximizing the likelihood of the sample of discrete velocities and positions, as detailed in DL08. For computing the likelihood, the particles and PNe are binned in elliptical segments, assuming an average projected ellipticity of 0.2. We consider 3 radial and 4 equally-spaced angular bins, with the first angular bin centered on the major axis, as shown in Fig. 7. Each segment contains at least 30 PNe.

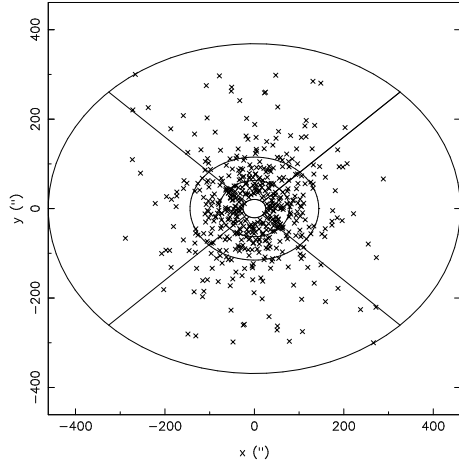


**Figure 7.** Segments in which the line-of-sight velocity distribution of particles is computed, for the likelihood method used to fit PNe with NMAGIC.

The number of independent data constraints for the different observables are  $J_{A_{lm}} = 450$ ,  $J_{S1} = 2390$ ,  $J_{Lets} = 346$ , and  $J_{PN} = 257$ . Since the errors are smallest for the  $A_{lm}$ , while the Poisson errors for the PNe are large, the  $A_{lm}$  terms contribute most to the force-of-change equation, while changes to the particle weights due the PNe data are small. To ensure that the halo is appropriately modelled, we increase the weight of the slitlets in the force-of-change by a factor of 4, and that of the PNe by a factor of 20. In practise we use the 4-folded data set for the slitlets (§2.2.2) and the 2-folded data set for the PNe (§2.2.3), so the actual weight factors in equation (4) are  $\xi_{A_{lm}} = \xi_{S1} = \xi_{Lets} = 1$ , and  $\xi_{PN} = 10$ .

### 3.5 Modelling procedure

Starting from the initial particle model described in Section 3.3, the weights of all particles are evolved by NMAGIC until the  $N$ -body system matches the target. During the whole evolution, the potential of the dark halo is kept fixed, but the stellar potential is frequently computed from the light distribution of the particle system. Particles are integrated in the total gravitational potential using a leapfrog scheme with adaptive time step.

After a relaxation phase of 1000 steps in which the initial particle model is advanced without any weight correction, particle weights are updated according to the force-of-change obtained maximizing equation (2), for  $\sim 10^5$  correction time steps. Finally, the particles are freely evolved for another  $10^4$  steps without any further weight correction, to ensure that the final particle model is well phase-mixed. For reference,  $10^4$  correction time steps correspond to  $\sim 300$  circular rotation periods at the target  $R_e$ . We define the model to have converged if  $\chi^2$  averaged over 50 steps stays almost constant in the last  $10^4$  steps, with fluctuations which are typically of order 2%.

During the weight adaptation, the model is regularized by the MPR method proposed in MG12. New priors are determined in phase-space as described in MG12, by binning particles according to their orbital integrals. In particular, we grid particles according to energy ( $E$ ), total circularity

$x$ , and angular momentum with respect to the rotation axis  $L_z$ , in a grid of  $n_E = 20$ ,  $n_x = 4$ ,  $n_z = 2$  bins, which at the same time resolves the relevant phase-space structures and ensures enough particles in each grid cell. The average weight contained in each cell is computed, and then a thin-plate smoothing spline is fitted to the grid of priors, before assigning them to the particles. The individual particle priors computed in this way are not kept constant in time but rather they are frequently updated while the particle weights are adapted to match the target observables.

## 4 PARAMETER ESTIMATION WITH NMAGIC: HOW WELL CAN THE DARK MATTER HALO BE RECOVERED?

In this work, we will be fitting the observational data of NGC 4494 with a sequence of NMAGIC models obtained for different dark matter halos and for different inclinations. In doing this, we wish to quantify the uncertainties in the best-fit parameters from a statistical distribution appropriate for our data and modelling method. In this Section, we describe a simple Monte Carlo method to estimate such a distribution.

In the following, the best-fit parameters are defined as those for which a minimum is achieved in the merit function

$$G = \frac{1}{2}\chi^2 - \mathcal{L}, \quad (8)$$

which measures the agreement between the independent observational data constraints and the final model in terms of the total  $\chi^2$  from  $A_{lm}$ , slits, and slitlets that the  $\chi^2$ M2M method tries to minimize, and of the log likelihood  $\mathcal{L}$  for the PNe that the method tries to maximize. In order to carry out a robust parameter estimation, we also need to quantify the uncertainties in these best-fit parameters.

Boundaries of the confidence regions for the estimated parameters will correspond to contours of constant  $\Delta G$  relative to the best-fitting model in the sampled parameter space. In common-practice dynamical mass analysis (see Introduction), uncertainties in the model parameters are typically estimated by considering the parameter change necessary to increase  $\chi^2$  by 1 (or 2.3), and to decrease the log likelihood  $\mathcal{L}$  (see DL08) by a factor of 0.5 (or 1.2) for 1 (or 2) fitted potential parameters (Press et al. 1992). This assumes Gaussian data, a model linear in its parameters, and that the number of fitted weight parameters  $N$  minus smoothing constraints  $N_s$  is less than the number of data points  $J$  so that the number of degrees-of-freedom  $N_{dof}$  is positive. In fact, the dependence on the potential parameters is non-linear, and in our models  $N \gg J$  so that  $N_{dof}$  may be less than zero. In addition, we find empirically for our data set and modelling set-up that  $\Delta\chi^2$  values are  $\gg 1$ . Therefore in this Section we compute confidence regions for parameter estimation via Monte Carlo experiments.

In Section 4.1, we build a mock target galaxy closely similar to the elliptical galaxy NGC 4494, which is embedded in a dark matter halo with scale radius and circular velocity corresponding to the best-fitting model determined by N09 for NGC 4494. We generate photometric and kinematic observables for this mock galaxy with the same observational errors as for NGC 4494. In Section 4.2, we use the pseudo-data and known intrinsic parameters of this NGC 4494-like

target galaxy to calibrate the regularization parameter appropriate for the modelling of NGC 4494. In Section 4.3, we determine how well the circular velocity and scale radius of the known dark halo, the total enclosed mass, and the mass-to-light ratio of the target galaxy can be recovered, in a more rigorous way than in previous NMAGIC modelling (DL08; DL09; Das et al. 2011). Finally, in Section 4.4 we use Monte Carlo experiments with such NGC 4494-like target galaxies to determine the appropriate  $\Delta G$  to be used for confidence boundaries. This will then allow us to quantify uncertainties in the dark halo mass distributions of the real NGC 4494 in Section 5.

#### 4.1 An NGC 4494-like galaxy and its observables

Our initial NGC 4494-like target galaxy has the luminosity distribution obtained by deprojecting the surface brightness of NGC 4494 for  $i = 90^\circ$ , and it is embedded in a logarithmic dark matter halo (equation (6), with  $r_0/R_e = 4$  and  $v_0 = 150 \text{ km s}^{-1}$ ), as in the best-fitting Jeans model of N09 for NGC 4494. Similar to the orbital anisotropy predicted by some merger models in the current cosmological scenario (*e.g.* Dekel et al. 2005), the velocity distribution of this NGC 4494-like galaxy is isotropic in the center and increasingly radially anisotropic at larger radii. As for NGC 4494, we observe the target galaxy from a distance of 15.8 Mpc, and the projected effective radius  $R_e \approx 49''$ . We set its stellar mass-to-light ratio to 3.8.

Following the procedure outlined in Section 3.3, we generate a spherical particle model realization for this target with 750000 particles. To implement the orbital anisotropy of the target galaxy, we adopt a model with specified circularity function following Gerhard (1991). We also add a certain amount of rotation to the particle model (see Section 3.3) so as to mimic the real NGC 4494. With this spherical model as starting point, we then use NMAGIC to evolve it to the edge-on luminosity distribution of NGC 4494. The resulting axisymmetric model galaxy is then used to compute mock observables.

As luminosity observables we use the coefficients  $A_{lm}$  of the spherical harmonic expansion of the 3D luminosity density, computed as described in Section 3.4. The kinematic observables are  $v, \sigma, h_3, h_4$ , projected onto both the long-slit set-up and the slitlets set-up used for the modelling of NGC 4494. These observables can be readily determined using NMAGIC with weight correction turned off, integrating the particle model for the target galaxy, and time-smoothing the observables (see MG12). Observational errors from NGC 4494 are adopted, and Gaussian random variates with  $1\sigma$  equal to these errors are added to the kinematic observables computed in this way.

Finally, we generate a mock sample of PNe velocities similar to that described in Section 2.2.3. We again use NMAGIC to integrate the particle model which imitates NGC 4494, and in parallel compute the time-averaged velocity and velocity dispersion of the particles binned in radial and angular segments on the sky. We adopt the same 3 radial bins and 4 equally-spaced angular bins as in Section 3.4. Then, we consider the catalogue of PNe used for the modelling of NGC 4494, and assign a new velocity to every PN in the catalogue, according to a Gaussian distribution with

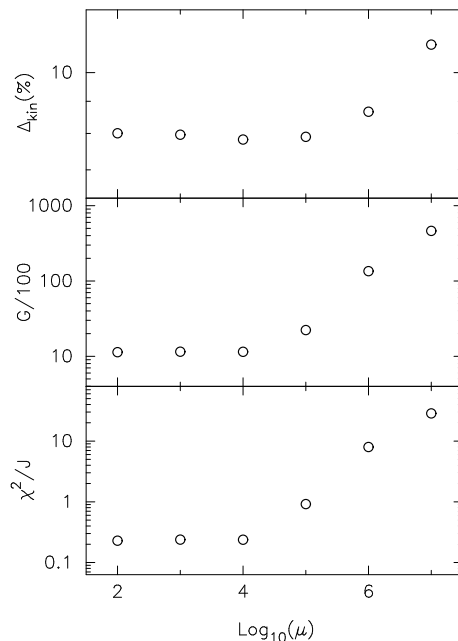


**Figure 8.** Quality parameters for the final NMAGIC particle models as a function of the regularization parameter  $\mu$ , from unsmoothed models (small values of  $\mu$ ) to oversmoothed models (high values of  $\mu$ ). *Top panel:* rms deviation (%) of the internal velocity moments of the final particle model from the target, computed over the radial region constrained by the data. *Middle panel:* merit function  $G$  in equation (8). *Bottom panel:*  $\chi^2/J$  of the particle model fit to the  $J = 3186$  photometric and absorption-line kinematic data points.

velocity and velocity dispersion of the spatial segment the PN would belong to, given its position on the sky.

#### 4.2 Calibrating regularization

The regularization parameter to be used when constructing dynamical models is case-dependent, and is influenced by several factors, most notably the observational data to be modelled (error bars, scatter, spatial coverage) and the phase-space structure of the target galaxy (see Gerhard et al. 1998; Cretton & van den Bosch 1999; Thomas et al. 2005, DL08; DL09; MG12).

To determine the optimal amount of smoothing given the data, we model the observational data of the NGC 4494-like galaxy using MPR (MG12), varying the regularization parameter  $\mu$  which controls the balance between regularization and goodness-of-fit in equation (2).

The results of our experiments are summarized in Fig. 8, which shows, for increasing values of  $\mu$ , the reduced  $\chi^2$ , the merit function  $G$  in equation (8), and the rms difference ( $\Delta_{kin}$ ) between the internal velocity moments of the target and of the final NMAGIC model (see MG12).

The minimum in the  $\Delta_{kin}$  plot determines the value of  $\mu$  for which the model best recovers the internal moments of the input model. This occurs at  $\mu \simeq 10^4$ . In Fig. 8 we also see that for values of  $\mu \geq 10^5$  a smooth model fitting the data points within errors can no longer be found.

Based on the results of these experiments, in the following we will adopt a value of  $\mu = 10^4$  to regularize our NMAGIC models.

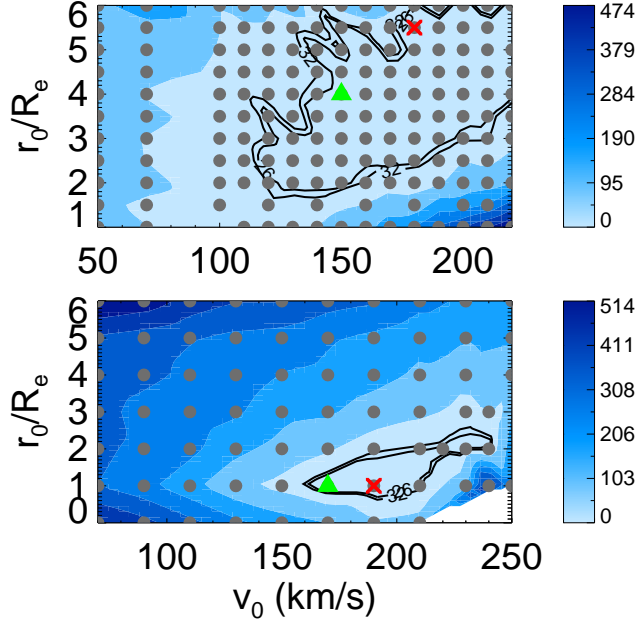


**Figure 9.** Recovering the halo parameters of NGC 4494-like galaxies. Each *circle* represents a final NMAGIC model. *Top panel:* the true dark halo (green triangle) has scale radius  $r_0 = 4R_e$  and circular velocity  $v_0 = 150 \text{ km s}^{-1}$ . *Bottom panel:* this more massive dark halo (green triangle) has scale radius  $r_0 = 1R_e$  and circular velocity  $v_0 = 170 \text{ km s}^{-1}$ . The colour scheme reflects the magnitude of the  $\Delta G$  of each model relative to the overall best-fitting model, defined as that with the smallest  $G$  (red cross). The black lines correspond to 70% and 90% confidence contours, as derived from the simulations of Section 4.4.

#### 4.3 Recovery of input parameters for the dark halo of an NGC 4494-like galaxy

We now construct NMAGIC models that fit the data of the NGC 4494-like target galaxy for a range of assumed parameters of the dark halo potential in equation (6). The key question that we are interested in is: how well can NMAGIC recover the true parameters of the dark halo given the observational data at hand?

We follow the modelling procedure outlined in Section 3.5, starting from an isotropic initial particle model computed in each dark halo, as explained in Section 3.3. We use all available photometric and kinematic constraints, including PNe through the likelihood technique. Our NMAGIC models are regularized with MPR, adopting the optimal value of  $\mu = 10^4$  determined above.

We sample the halo parameters  $(r_0, v_0)$  on a grid of  $\sim 200$  models. The results of these experiments are shown in the top panel of Fig. 9 in terms of the  $\Delta G$  of each NMAGIC model relative to the best-fitting model, which corresponds to the overall smallest  $G$ . The shape of the  $\Delta G$  contours is regular, and there is an extended region for which the values of  $G$  are similar. Many models for different parameters of the dark halo provide similarly good fits to the data, all with  $\chi^2/J \leq 1$  (the number of data points entering  $\chi^2$  is  $J = 3186$ ).

The best-fitting model is found for values of the dark halo parameters  $r_0 = 5.5R_e$  and  $v_0 = 180 \text{ km s}^{-1}$ , and it has

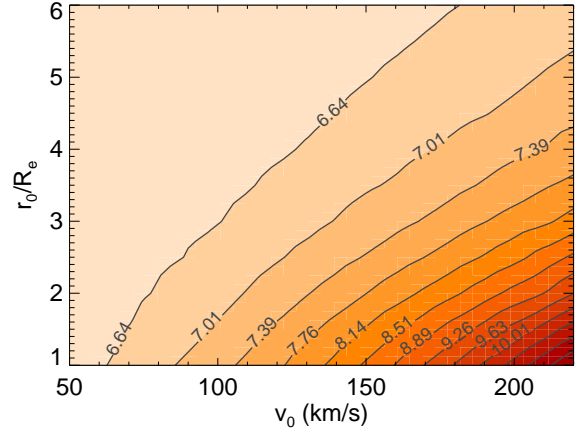


**Figure 10.** Total enclosed mass within  $2R_e$  (stars plus dark matter) for different values of the halo parameters  $r_0$  and  $v_0$ . Contour values are in units of  $10^{10} M_\odot$ .

$\chi^2/J = 0.22$ , log likelihood  $\mathcal{L} = -770.5$ , and  $G = 1125.6$ . The scale radius of this best-fitting model is larger than that of the true model, which achieves  $\chi^2/J = 0.24$ , log likelihood  $\mathcal{L} = -769.9$ , and  $G = 1148.7$ . For comparison, the no-dark halo model, which provides the poorest fit to the available observational data, has a final  $\chi^2/J = 0.37$ , log likelihood  $\mathcal{L} = -782.2$ , and  $G = 1376.6$ .

Surprisingly, the values of  $\Delta G$  are large ( $\gg 1$ ). For instance, the model obtained for the true parameters of the (known) dark matter halo achieves a value of  $G$  which is  $\Delta G \sim 20$  ( $\Delta\chi^2 \sim 60$ ) away from the best-fitting model. Applying the classical  $\chi^2$  statistics for two degrees of freedom, the true parameters of the dark matter halo would be discarded at the 99.99% level. We investigate this issue in Section 4.4.

Note that the contours of  $\Delta G$  remain open to the top-right edge of the plot (see also *e.g.* Gerhard et al. 1998; Thomas et al. 2005; Murphy et al. 2011), showing that it is not possible to put robust constraints on both halo parameters simultaneously in this case. Similar values of  $G$ , and hence similarly good models are achieved for halo models located along a large band extending from low  $r_0$  and low  $v_0$  to high  $r_0$  and high  $v_0$ .

This diagonal band shrinks when modeling target galaxies embedded in more massive halos, as the models that do not contain enough mass are then ruled out. This is shown in the bottom panel of Fig. 9, which is obtained by repeating the analysis for an NGC 4494-like galaxy embedded in a more massive dark matter halo (whose parameters are set to  $r_0 = 1R_e$  and  $v_0 = 170 \text{ km s}^{-1}$ ).

Models inside the diagonal band share a similar total enclosed mass within the radial region constrained by the observational data, as shown in Fig. 10 by means of contours of total mass within  $2R_e$  in the same  $(r_0, v_0)$  parameter space. Evidently, the total enclosed mass inside a certain radius is what the dynamical models constrain best with the data at hand. Indeed, when plotting the values of  $\Delta G$  of the final NMAGIC models against enclosed mass (see Fig. 11) the shape of a parabola is evident, despite the scatter in the values of  $\Delta G$ .

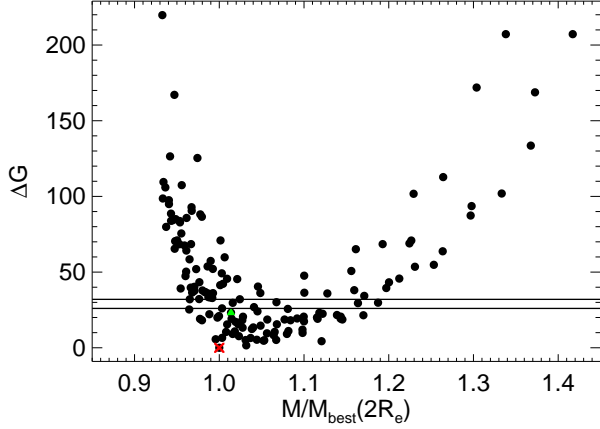


**Figure 11.**  $\Delta G$  of the final NMAGIC models fitting the data of the NGC 4494-like galaxy, as a function of the total mass inside  $2R_e$  divided by the corresponding quantity for the best-fitting model. The *red cross* shows the best-fitting model, the *green triangle* the model with the true dark halo parameters ( $r_0 = 4R_e$ ,  $v_0 = 150\text{kms}^{-1}$ ). The black lines correspond to 70% and 90% confidence regions derived from the simulations of Section 4.4.

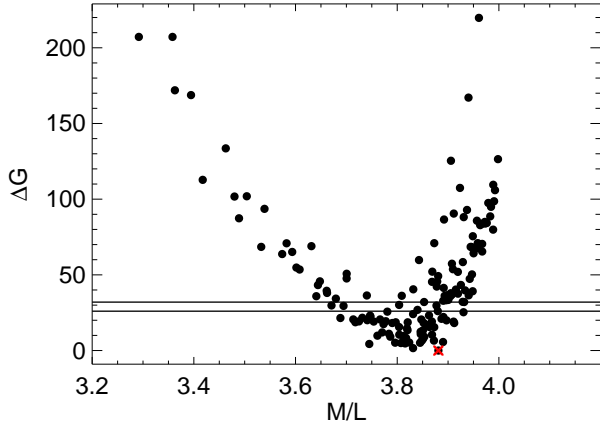


**Figure 12.** As Fig. 11, but  $\Delta G$  of the final NMAGIC models as a function of stellar mass-to-light. The galaxy has (known)  $M/L = 3.8$ .

Figs. 12-13 show how well the NMAGIC models recover the mass-to-light ratio and dark matter fraction of the NGC 4494-like galaxy from the mock data. These are both important quantities which we are interested in measuring with accuracy for real galaxies.

At this stage, two obvious questions are: what is the typical  $\Delta G$  difference between the best-fitting NMAGIC model and the model with the true halo parameters? And related to this, within what errors can we trust the dark halo parameters of the best-fitting model? The following analysis is designed to answer these questions.

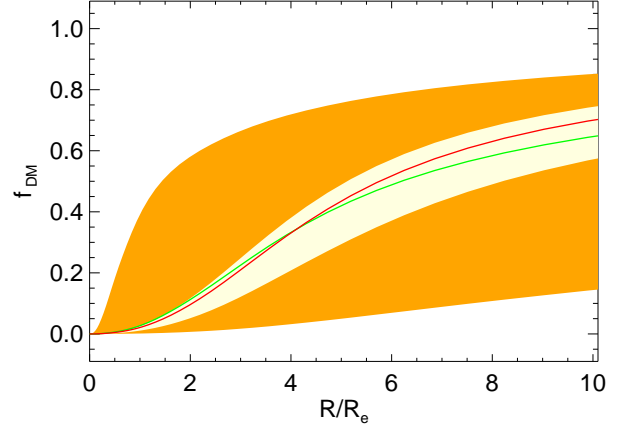


**Figure 13.** Recovery of the dark matter fraction  $f_{\text{DM}} = M_{\text{DM}}/M$  as a function of radius for the range of explored NMAGIC models of the NGC 4494-like data (*orange shaded region*). The *green line* represents the known target, and the *red line* the best-fitting model. The *yellow shaded region* shows the 70% confidence region (see Section 4.4).

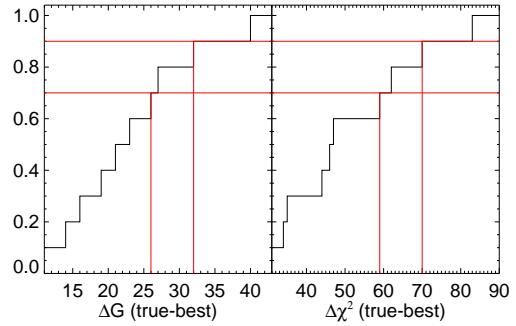


**Figure 14.** Normalized cumulative distribution of  $\Delta G$  (left) and  $\Delta\chi^2$  (right) between the true dark halo and the best fitting model, derived from NMAGIC models of the NGC 4494-like galaxy embedded in 10 different dark halos. The best fitting model is defined as that with the minimum  $G$  ( $\chi^2$ ). The *red lines* correspond to 70% and 90% confidence levels.

#### 4.4 Parameter estimation for the dark matter halo: confidence levels

We use Monte Carlo simulations to estimate the values of  $\Delta G$  which represent a specific confidence level, given the observational data of NGC 4494 and our NMAGIC modelling technique.

In practice, given constraints on computer time, we construct a sequence of NGC 4494-like galaxies embedded in 10 different dark halos, and model each one of them with a range of dark halo parameters. Then, for each target galaxy we compute the  $\Delta G$  between the best-fitting model and the model obtained for the true parameters. In this way, we can estimate the values of  $\Delta G$  within which the true parameters are found in 70% or 90% of our experiments.

The main results from these experiments are summarized in Fig. 14, which shows the cumulative distributions

of  $\Delta G$  and  $\Delta\chi^2$  between the true dark halo model and the best fitting model, for the 10 different experiments. It is seen that the NMAGIC models recover the true potential of the dark matter halo within  $\Delta G \lesssim 26$  about 70% of the time, and within  $\Delta G \lesssim 32$  about 90% of the time. Corresponding values when the log likelihood is not included are:  $\Delta\chi^2 \lesssim 59$  and  $\Delta\chi^2 \lesssim 70$  for 70% and 90% confidence regions, respectively.

The magnitude of these differences is quite surprising. Therefore we perform several additional tests to understand them better. First, we verify that the measured differences  $\Delta G$  are actually significant with respect to fluctuations caused by modelling noise or measurements uncertainties. Indeed, it is natural to speculate that the numerical noise in the procedure of the weight-adjustment may cause fluctuations of  $G$  over time. However, these fluctuations are comparatively small; on average they are  $\sim 8$  in  $G$  ( $\sim 17$  in  $\chi^2$ ), i.e. a factor of three smaller than the typical values of  $\Delta G$  (and  $\Delta\chi^2$ ).

Then, in order to quantify the relevance of the observational measurement uncertainties, we generate a Monte Carlo chain of one hundred realizations of the data of the NGC 4494-like mock galaxy of Section 4.1. Every realization is constructed by drawing random Gaussian-distributed values for all kinematic data points, such that the mean is as predicted for the mock galaxy, and the variance corresponds to the observational errors (see *e.g.* van der Marel et al. 1998; Cretton et al. 2000; Thomas et al. 2005). Then, we model each realization with NMAGIC, assuming the true gravitational potential of the target galaxy. Based on modeling 100 realizations of the observational data, we conclude that random variations in the data according to the observational errors correspond to fluctuations of  $\sim 16$  in the merit function  $G$  (and  $\sim 32$  in  $\chi^2$ ) within  $1\sigma$ . Instead, the experiments above showed that if the potential is not known in advance, NMAGIC models match the true potential of the dark matter halo within  $\Delta G \lesssim 26$  at  $1\sigma$  level. Hence, the  $\Delta\chi^2$  difference derived from only fitting data sets of the true model (*e.g.* Thomas et al. 2005) appears to be an underestimate.

As a further check, we verify whether the minimum value of  $G$  and/or the magnitude of  $\Delta G$  are influenced by the degree of regularization employed in the NMAGIC fits. In the framework of Schwarzschild modelling, Verolme et al. (2002) showed that smoothing constraints do not affect the shape of  $\chi^2$ -contours significantly, and leave the overall best-fitting parameters unchanged. Thomas et al. (2005) constructed Schwarzschild models for different values of the smoothing parameter, and computed the  $\Delta\chi^2$  due to  $N_{\text{mock}} = 60$  different realizations of the data sets as a function of the smoothing parameter. They found that the magnitude of  $\Delta\chi^2$  increases for increasing regularization (see their Fig. 6). We repeat their experiment modelling  $N_{\text{mock}} = 100$  realizations of the data of the NGC 4494-like mock galaxy for different values of the regularization parameter  $\mu$ , and show our results in Fig. 15. The error bars represent the  $1\sigma$ -variation  $\Delta G$  as a function of  $\mu$  (note that they are multiplied by a factor 5), and show no indication that such  $\Delta G$  is influenced by the regularization, up until and including the optimal regularization parameter used in our modeling ( $\mu = 10^4$ ). An increase of the fluctuations of  $G$

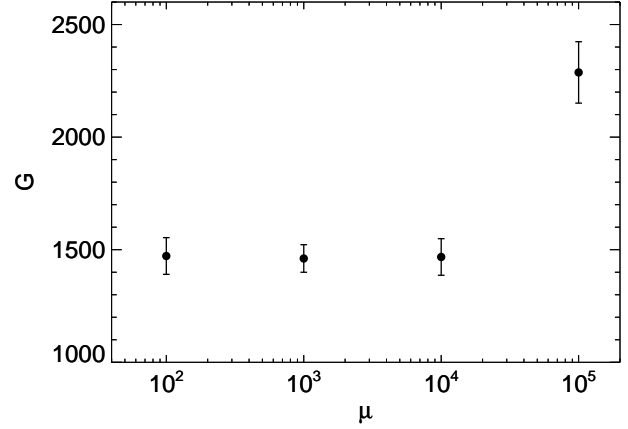


**Figure 15.** The merit function  $G = \chi^2/2 - \mathcal{L}$  for increasing values of the regularization parameter  $\mu$ . Dots represent the mean over 100 model fits to Monte Carlo realizations of the kinematic data of the NGC 4494-like galaxy; error bars represent the rms deviation from the mean multiplied by a factor 5.

due to regularization is only seen for oversmoothed models ( $\mu = 10^5$ , see Section 4.2).

The Monte Carlo experiments also reveal some slight biases which are intrinsic to our diagnostics of the best-fitting model. In particular, we find that the minimum  $\chi^2$  values are achieved on average for slightly more massive halos than that of the target galaxy, as previously noted in Gerhard et al. (1998), while the maximum  $\mathcal{L}$  values are typically achieved for halos which are slightly more diffuse than the true (known) halo. The combination of  $\chi^2$  and  $\mathcal{L}$  in the merit function  $G$  in equation (8) is less biased, since it strikes a compromise between these two opposite trends.

#### 4.5 Summary

To summarize, we investigated how well the dark halo parameters can be constrained from data which have the spatial coverage and error bars of the current observational data for NGC 4494. These data do not suffice to determine uniquely both the scale radius and the circular velocity of the halo specified in equation (6), and different combinations of  $(r_0, v_0, \Upsilon)$  that yield similar values of the total enclosed mass are allowed. The enclosed mass within  $2R_e$  can be determined to within 10%, and the dark matter fraction  $f_{\text{DM}}(3R_e)$  to within  $\pm 0.1$ . For the family of logarithmic dark matter halos, the total circular velocity can be determined to  $\pm 20 \text{ km s}^{-1}$ .

Via Monte Carlo experiments, we computed confidence levels for parameter estimation. We conclude that, for NMAGIC models of the observational data at hand, the usual  $1\sigma$  (70%) level corresponds to a value of  $\Delta G \sim 26$ , and of  $\Delta\chi^2 \sim 59$  (and  $\Delta G \sim 32$ ,  $\Delta\chi^2 \sim 70$  at 90% confidence level). Using these statistical results, we can now derive the uncertainties on the determination in the halo parameters for NGC 4494.

## 5 DYNAMICAL MODELS OF NGC 4494

We now use NMAGIC to construct axisymmetric dynamical models for NGC 4494 fitting all the photometric and kinematic data described in Section 2. Three different inclinations for the stellar distribution are considered,  $i = 90^\circ, 70^\circ, 45^\circ$ , for which we carried out the deprojection of the photometric data (see Section 2.1). The latter value is close to the minimum inclination allowed by the observed flattening of NGC 4494 (N09; F11). For each inclination, we explore a sequence of gravitational potentials, including the self-consistent case with constant  $M/L$  and various quasi-isothermal dark matter halos.

The main results of our suite of dynamical models are presented in Fig. 16. In analogy with the analysis of the previous Section, we plot the  $\Delta G$  of each NMAGIC model relative to the best-fitting model, defined as that with minimum  $G$ , for each inclination  $i = 90^\circ, 70^\circ, 45^\circ$ . For reference, the best-fitting model for  $i = 90^\circ$  has  $\chi^2/J = 0.41$ , log likelihood  $\mathcal{L} = -793.3$ , and  $G = 1449.2$ . In the same figure, we also overplot the 70% and 90% confidence levels determined from the Monte Carlo experiments of Section 4.4. In the right panel, we show the final mass-to-light ratios of our dynamical models.

The shape of the  $\Delta G$ -contours is regular, and the range of dark matter halos consistent with the data within the confidence levels has circular velocity in  $[160-240] \text{ km s}^{-1}$  and scale radius  $\sim 1-2R_e$ . The stellar mass-to-light ratio is  $\Upsilon_V \sim 3$ . The main characteristics of the mass distribution of the explored models, and of the preferred models, are plotted in Fig. 17. The total circular velocity curve of the good models is approximately flat (“isothermal”) outside  $1R_e$ , with  $v_c(3R_e) \sim 220 \text{ km s}^{-1}$ . Less massive halos, as well as models with constant  $M/L$ , are not consistent with the data.

It is apparent from Fig. 16 that these main results, and the topology of the contours of  $G$ , are independent of the adopted inclination of the stellar distribution of NGC 4494. In general, we find that edge-on models ( $i = 90^\circ$ ) are preferred, in the sense of a lower value of  $G$ , a lower value of  $\chi^2$ , and a higher value of  $\mathcal{L}$ , respectively. A discussion of this issue is deferred to Section 5.3, whereas we now describe the model fits to the data, and the orbital structure of the dynamical models.

### 5.1 Model fits to the observational data

For a wide range of dark halos, NMAGIC finds very good fits to the observational data in terms of  $\chi^2$  values. In particular, for all the assumed values of the inclinations, the models embedded in the dark matter halos that that we tried converged to  $\chi^2/J$  values per data point less than 1 (except for extreme values of the parameters, corresponding to the bottom-right corner of Fig. 16). The models with constant  $M/L$  achieve the poorest fit, with a value of reduced  $\chi^2/J = 0.60$  ( $90^\circ$ ),  $\chi^2/J = 0.94$  ( $70^\circ$ ), and  $\chi^2/J = 1.15$  ( $45^\circ$ ).

The fits to the photometric constraints are generally excellent, and they are visually indistinguishable for most potentials, and for the different inclinations. Models compatible with the data at the 90% level achieve these fits with a maximum value of  $\chi^2/J_{A_{lm}} = 0.43, 0.48, 0.88$ , for

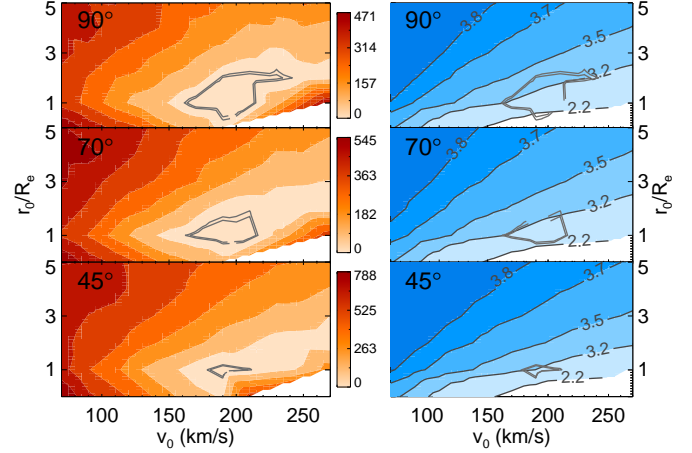


**Figure 16.** Results of the NMAGIC dynamical models of NGC 4494 for the range of explored halo parameters  $(r_0, v_0)$ . *From top to bottom:*  $i = 90^\circ, 70^\circ, 45^\circ$ . The grey contours correspond to 70% and 90% confidence levels, as determined in Section 4.4. *Left column:*  $\Delta G$  of NMAGIC models relative to the best-fitting model (separate colour bar for each inclination). The bottom-right corner is a region in which no good models for the data could be found. *Right column:* V-band mass-to-light  $\Upsilon_V$  of the final models.

$i = 90^\circ, 70^\circ, 45^\circ$ , respectively. Fig. 18 shows the very good fit to the first moment of the  $A_{lm}$ , i.e. the differential stellar mass distribution, for the preferred inclination of  $90^\circ$ . Three fiducial halo models are shown: the best-fitting model, and two models which fit the data with  $\chi^2 < 1$ , but lie outside the 90% confidence band, having a more massive and a more diffuse dark halo than the best-fitting models.

The fits to the long-slit kinematics are also generally good. Models within the 90% confidence range achieve a maximum value of  $\chi^2/J_{sl} = 0.36, 0.41, 0.35$ , for  $i = 90^\circ, 70^\circ, 45^\circ$ , respectively. For the fiducial models, these fits are shown in Fig. 19, where it is apparent that the central feature of the kinematically decoupled core in  $v$  and in  $h_3$  is reproduced well by our particle models, and that the models have some difficulty in matching the detailed long-slit kinematics along the outer major axis. In particular, the best-fitting models have slightly lower values of  $v$  and slightly higher values of  $\sigma$ . To a great extent, these systematic deviations can be traced to the compromise that the models must find (see below) between the long-slit and the slitlets kinematic data, which extend to larger radii. The fiducial models show that more massive/diffuse halos result in higher/lower values of  $\sigma$  and  $h_4$  along both axes. Finally, the shaded regions in Fig. 19 show the range of models allowed by the different inclinations (for the more massive and the more diffuse fiducial models), and by the 90% confidence region (for the best-fitting model).

The fits to the newer slitlets kinematics are achieved with maximum  $\chi^2/J_{lets} = 1., 1.18, 1.27$  within the 90% confidence level, for the three inclinations of  $90^\circ, 70^\circ, 45^\circ$ , respectively. Fig. 20 shows the fits of the preferred edge-on particle models to the slitlets kinematics for the fiducial potentials. The trends with halo mass described before are still clearly visible. Moreover, it can be seen that the best-fitting edge-on model, corresponding to the black line, has to find

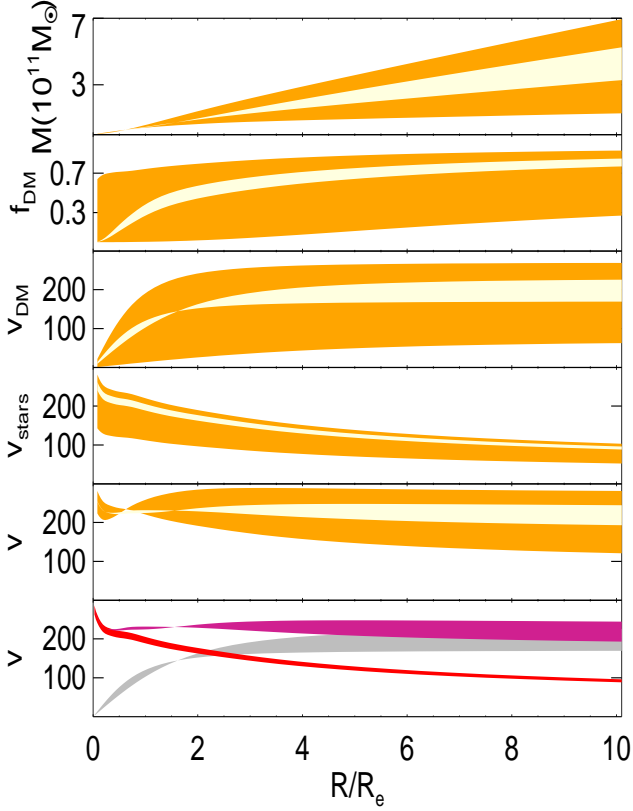


**Figure 17.** *Top five panels:* as a function of radius, the total mass, the dark matter fraction  $f_{\text{DM}} = M_{\text{DM}}/M$  within  $R$ , and the circular velocity curves corresponding to dark matter, stars, and total potential. The *orange shaded region* shows all edge-on NMAGIC models investigated, the *yellow shaded region* shows the 70% confidence region (see Section 4.4). *Bottom panel:* the contributions of stars (*red*) and dark matter (*grey*) to the total circular velocity curve (*violet*) for the edge-on models in the 70% confidence band.

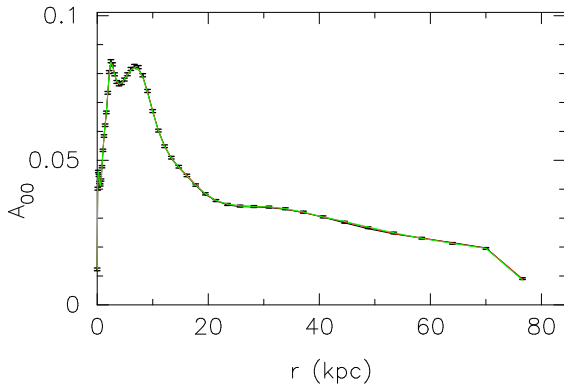


**Figure 18.** NMAGIC fits to the differential stellar mass distribution ( $A_{00}$  coefficient) for an inclination of  $90^\circ$ . The *black line* is for the best-fitting model ( $r_0 = 1R_e$ ,  $v_0 = 190\text{kms}^{-1}$ ), the *red line* is for a model residing in a more diffuse halo ( $r_0 = 5R_e$ ,  $v_0 = 90\text{kms}^{-1}$ ), and the *green line* represents a model obtained for a massive halo ( $r_0 = 1R_e$ ,  $v_0 = 250\text{kms}^{-1}$ ). The three model curves are nearly identical even though the last two models are outside the 90% confidence region.

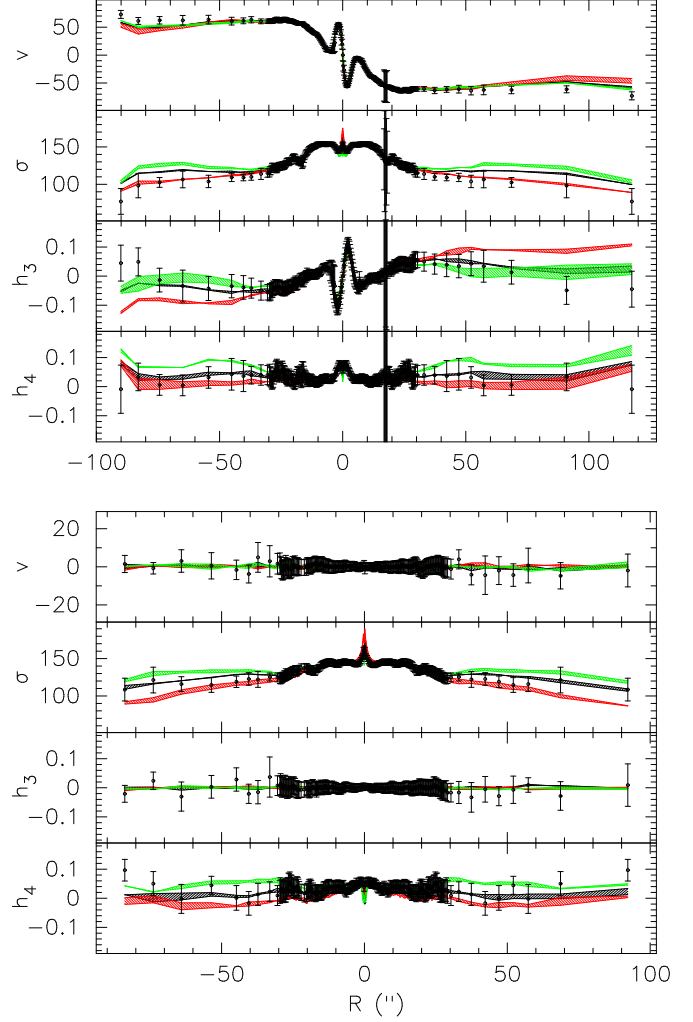


**Figure 19.** NMAGIC fits to the long-slit kinematic data (*black dots*) of NGC 4494 along the major (*top*) and minor (*bottom*) axis. The *black shaded region* shows the best-fitting edge-on models within the 90% confidence range. The *red and green shaded regions* show the spread of two fiducial models for the explored inclinations; *red* is for the model residing in a lighter halo ( $r_0 = 5R_e$ ,  $v_0 = 90\text{kms}^{-1}$ ), and *green* is for the model obtained in a massive halo ( $r_0 = 1R_e$ ,  $v_0 = 250\text{kms}^{-1}$ ). Both models are well outside the confidence range.

a compromise between the kinematic data in slit and slitlets in the outer region. This results in a lower magnitude for the velocity, and in a higher velocity dispersion, which explains the deviations from the long-slit kinematics in the outermost data points.

Finally, Fig. 21 shows a comparison of the final NMAGIC models with the PN kinematic data, for all the inclinations and for the fiducial potentials. The velocity, velocity dispersion, and LOSVD are plotted in the angular segments used for the modelling (see Section 2.2.3). The axisymmetric nature of our models is apparent in the reflection symmetry of the kinematics in diagonally opposite segments. While the mean velocity profiles are well fit by all models shown, the low (high) dark matter models are systematically low (high) in the PN dispersion plot, and show systematic deviations from the data histograms. The best-

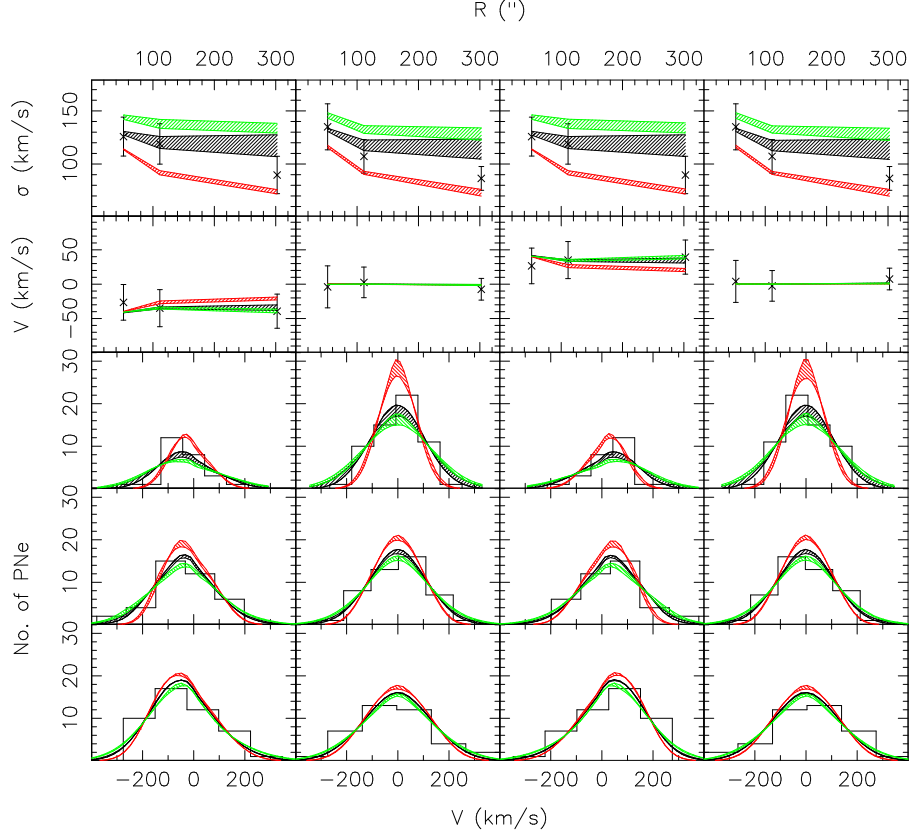


**Figure 21.** NMAGIC fits to the PNe velocities for all the considered inclinations. *Top two rows:* mean velocity dispersion and velocity profiles in the angular segments centered on  $0^\circ$  (major axis),  $90^\circ$ ,  $180^\circ$ ,  $270^\circ$ , from left to right. *Bottom three rows:* LOSVD in the same angular segments at radii of  $52''$ ,  $110''$ , and  $300''$ , going upwards. Colours of the *shaded regions* are as in Fig. 19.

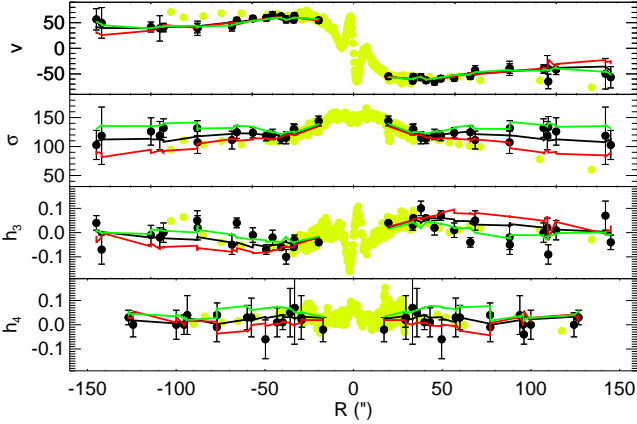


**Figure 20.** NMAGIC fits to the slitlets kinematics near the major axis of NGC 4494 (*black dots* with error bars). For comparison, *light-green dots* represent the original major-axis slit data. The model points are averages over the same slit cells as the data, and are connected by straight line segments. Different colours represent the fiducial models: *black* is for the best-fitting model ( $r_0 = 1R_e$ ,  $v_0 = 190\text{kms}^{-1}$ ), *red* is for the model residing in a lighter halo ( $r_0 = 5R_e$ ,  $v_0 = 90\text{kms}^{-1}$ ), and *green* is for the model obtained in a massive halo ( $r_0 = 1R_e$ ,  $v_0 = 250\text{kms}^{-1}$ ). For simplicity, only the preferred edge-on models are shown.

fitting models, instead, provide a good match to all the PN data.

## 5.2 The internal kinematics of NGC 4494

We now look at the intrinsic kinematics of the NGC 4494 models, in order to learn about the orbital anisotropy of this galaxy. Fig. 22 shows the internal kinematics for the range of explored inclinations.

As expected, in the radial region well constrained by the kinematic data the ratio of the radial to tangential velocity dispersions is larger for models embedded in a massive halo than for low dark matter models (see *e.g.* Binney & Mamon 1982; Gerhard 1993).

On average, the ratio of the radial to tangential velocity dispersions along  $R$  in the best-fitting models is  $\sim 1.2$ , i.e. the underlying orbital distribution is slightly radially biased. As discussed further in Section 6, the degree of radial anisotropy of NGC 4494 is milder than what was previously found for the two other intermediate-luminosity ellipticals NGC 4697 (DL08) and NGC 3379 (DL09).

For all the explored potentials, the two components of the tangential velocity dispersion are similar along the minor axis, as required for an axisymmetric system, whereas the azimuthal dispersions are higher in the equatorial plane, suggesting together with the radial anisotropy that this (rotating) elliptical may be flattened by meridional anisotropy (*e.g.* Dehnen & Gerhard 1993; Thomas et al.

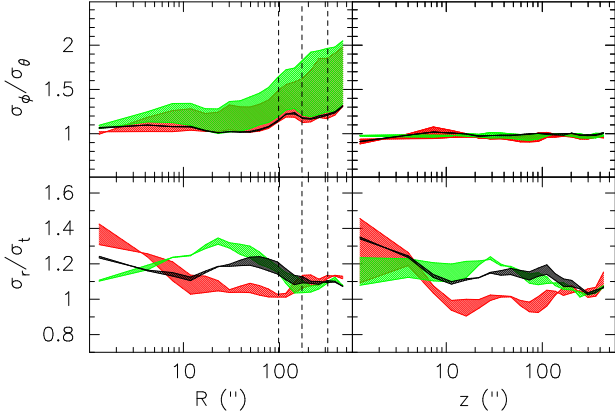


**Figure 22.** Internal kinematics of the final NMAGIC models for NGC 4494. The ratio of the azimuthal to meridional velocity dispersion  $\sigma_\phi/\sigma_\theta$  (top) and of the radial to tangential velocity dispersion  $\sigma_r/\sigma_t = \sqrt{(\sigma_\theta^2 + \sigma_\phi^2)/2}$  (bottom) are plotted as a function of major axis  $R$  in the equatorial plane (left column), and of minor axis  $z$  in the meridional plane (right column). Colours of the shaded regions are as for Figs. 19, 21. The vertical dashed lines show the extent of the kinematic data (long-slit, slitlets, and PNe, going outwards).

2009a; Das et al. 2010b). Variations due to the assumed inclination are always larger in the ratio between the azimuthal and meridional velocity dispersions along  $R$ .

Finally, at larger radii, and close to the outermost data points (marked by the vertical dashed lines), the orbital structure is nearly isotropic along both  $R$  and  $z$ . As we have shown in MG12, in those external regions, which are unconstrained by the observational data, a bias towards the dynamical structure of the initial (isotropic, in this case) particle model cannot be avoided.

### 5.3 The inclination of NGC 4494

From our NMAGIC models of NGC 4494, we would conclude that the observational data prefer an inclination of  $90^\circ$  out of the three inclinations that we explored. Indeed, edge-on models provide better fits to the data than models with lower inclinations, in terms of the merit function  $G$ , as well as  $\chi^2$  and  $\mathcal{L}$ . In particular, we find a  $\Delta G \sim 144$  (78) between the best-fitting edge-on model and the best-fitting model obtained for  $45^\circ$  ( $70^\circ$ ), which is highly significant when compared to the typical differences  $\Delta G$  among different potentials for a given inclination. Visually, it is hard to distinguish the fit to the observables for the  $90^\circ$  and the  $70^\circ$  inclinations, whereas the more face-on  $45^\circ$  models are characterized by a systematically low velocity and velocity dispersion with respect to the observational data.

Should this preference for edge-on inclinations really be believed? Up to now, we have assumed a spherical dark halo for all the considered inclinations, and only the stellar distribution was axisymmetric and varied according to the inclination. We can relax the assumption of sphericity of the dark matter halo, and investigate dark matter halos with similar flattening as for the stars. To this end, we consider the flattened logarithmic potential

$i_G$	$i_M$	$\chi^2$	$G$	$-\mathcal{L}$
$90^\circ$	$90^\circ$	0.24	1148.74	769.93
$70^\circ$	$70^\circ$	0.27	1195.40	767.99
$45^\circ$	$45^\circ$	0.35	1313.38	754.93
$90^\circ$	$70^\circ$	0.26	1178.91	769.84
$90^\circ$	$45^\circ$	0.38	1371.26	770.90
$45^\circ$	$70^\circ$	0.30	1228.82	756.56
$45^\circ$	$90^\circ$	0.29	1218.26	756.86

**Table 1.** Results of NMAGIC fits to an NGC 4494-like galaxy whose stellar distribution has a known inclination  $i_G$ , assuming an inclination  $i_M$  in the modelling.  $\chi^2$  values are normalized by the number of observables  $J = 3186$ .

$$\phi_D(R, z) = \frac{v_0^2}{2} \ln \left( r_0^2 + R^2 + \frac{z^2}{q_\phi^2} \right) \quad (9)$$

(Binney & Tremaine 2008). Then, we use the approximate relation  $1 - q_\phi \sim (1 - q_\rho)/3$  to derive the flattening of the potential  $q_\phi$  from that of the density distribution  $q_\rho$ , which we infer from the apparent flattening  $q$  of the isophotes via

$$q^2 = \cos^2 i + q_\rho^2 \sin^2 i. \quad (10)$$

For an average flattening of the isophotes  $q = 0.82$ , the intrinsic flattening of the density distribution  $q_\rho = 0.82, 0.79, 0.59$  for  $i = 90^\circ, 70^\circ, 45^\circ$ , respectively, and the corresponding  $q_\phi = 0.94, 0.93, 0.86$ .

We have explored a few flattened dark halos with these parameters and the same spherically-averaged mass distribution as the best-fitting models for  $i = 70^\circ$  and  $45^\circ$ . Although some of them provide slightly better fits to the observational data, our main result does not change, and edge-on models are still preferred by far.

The obvious next question is whether there could be some bias in the modelling technique. This explanation was proposed by Thomas et al. (2007a), who found that all their best-fitting Schwarzschild models of  $N$ -body merger remnants have  $i = 90^\circ$ , and argued that edge-on models necessarily have a smaller  $\chi^2$  than face-on models, due to their greater freedom in the adjustment of prograde and retrograde orbits to fit rotation and axisymmetric deviations from a Gaussian LOSVD.

We used our NGC 4494-like galaxy (see Section 4.1) to test whether particle models exhibit a bias analogous to that of orbit-based models. First, we constructed a series of NGC 4494-like galaxies assuming different inclinations  $i_G = 90^\circ, 70^\circ, 45^\circ$  for the stellar distribution. Then, we modelled the observational data of these mock galaxies with NMAGIC for different inclinations  $i_M$ . The results of these experiments are summarized in Table 1, and confirm the findings and the argument of Thomas et al. (2007a): on average, the values of  $\chi^2$ , and of the merit function  $G$ , increase for lower values of the inclination. Table 1 reveals that edge-on models generally provide better fits. This is true both in the case in which the model has the true known inclination of the target galaxy, and in the case in which the model assumes a wrong value of the inclination. For reasons that are currently unclear to us, the likelihood favours instead more face-on models.

This test does not only confirm the existence of a bias (e.g., Thomas et al. 2007a), but also enables us to quantify its effect on the dynamical models of NGC 4494. The exper-

iments show that, when modelling a NGC 4494-like galaxy which has a true inclination  $i_G = 45^\circ$ , a  $\Delta G \sim 95$  between the edge-on model and the more inclined model could be associated with the “edge-on bias”. However, our NGC 4494 runs display a significantly larger difference  $\Delta G \sim 144$  between the edge-on and the  $i_M = 45^\circ$  models. Thus, combining these results suggests that NGC 4494 is truly close to edge-on. If so, this might provide also a simple explanation for the slightly larger rotation velocities measured in the major axis slit compared to the surrounding slitlets (see Fig. 20). This could be the kinematic signature of a faint disk.

## 6 DISCUSSION

In this Section we discuss (i) the results on parameter estimation of dark matter halos with NMAGIC, (ii) our dynamical models for NGC 4494 in comparison with previous work, and (iii) the dark matter distribution and orbital structure of NGC 4494 in the wider context of intermediate-luminosity elliptical galaxies with steeply falling, ‘quasi-Keplerian’ velocity dispersion profiles.

### 6.1 Confidence limits for parameter estimation with NMAGIC

In Section 4 we used Monte Carlo simulations of a NGC 4494-like mock galaxy in different dark matter haloes to assess the confidence limits for the halo parameters that provide statistically valid models for the real NGC 4494. The data set for the mock galaxy closely resembled that of NGC 4494. We estimate the differences in the merit function  $\Delta G$  corresponding to confidence levels enclosing a certain probability of finding the true values of the parameters (*e.g.* Press et al. 1992; Thomas et al. 2005). Specifically, we constructed and modelled 10 NGC 4494-like galaxies in different dark matter halos, and estimated the distribution of  $\Delta G$  values between the best-fitting model and the model with the true halo parameters for our data and modelling set-up.

These experiments showed that our NMAGIC dynamical models match the true potential of the dark matter halo within  $\Delta G \lesssim 26$  ( $\Delta\chi^2 \lesssim 59$ ) about 70% of the time, and within  $\Delta G \lesssim 32$  ( $\Delta\chi^2 \lesssim 70$ ) about 90% of the time. These values also correspond approximately to the fluctuations found within the confidence boundaries. The numerical noise in  $G$  or  $\chi^2$  caused by the adjustment of particle weights explains only a minor fraction of these  $\Delta G$  or  $\Delta\chi^2$  fluctuations. Fluctuations induced by varying the data within their error bars are much more significant compared to the measured  $\Delta G$  or  $\Delta\chi^2$  values, as already noted by Thomas et al. (2005) in the context of Schwarzschild’s method. Our experiments show, however, that some additional uncertainty must be related to the freedom associated with comparing different trial potentials. They also indicate that these results are unaffected by the strength of regularization as long as the model is not oversmoothed.

The relative differences  $\Delta G$  (and  $\Delta\chi^2$ ) found in our simulations are substantially larger than what is often assumed, and reveal that the  $\Delta\chi^2 = (1, 2.3, \dots)$  criterion for  $\nu = (1, 2, \dots)$  free model parameters used in many dynamical

studies in the literature (see Introduction) is inappropriate for our NMAGIC particle models.

The  $\Delta\chi^2(\nu)$  approach in dynamical modelling is based on  $\chi^2$ -statistics and assumes Gaussian errors, linear dependence on the model parameters, and that the number of degrees of freedom is positive (*e.g.* Press et al. 1992). Then  $\chi^2$  can be marginalized over all degrees of freedom other than the number of free parameters in the mass model. This implies the assumption that much of the freedom in the fitted weights (or orbits) is used by the regularization in constraining the distribution function from the data in the given trial potential. Because the number of particle weights is much larger than the number of data points, and given the indications that the simulations results are insensitive to the regularization parameter (Section 4.4), this assumption could be incorrect.

The  $\Delta\chi^2$  values found in our experiments appear to be larger than in typical Schwarzschild applications. One exception appears to be the work of van den Bosch & van de Ven (2009) who determined confidence limits on the modelling parameters based on the expected standard deviation of  $\chi^2$  itself,  $s(\chi^2) = \sqrt{2(J - M)}$ , where  $J$  is the number of observational constraints and  $M = 4$  the number of their free model parameters. However, the fact that the standard deviation of  $\chi^2$  is  $s(\chi^2)$  does not invalidate the standard  $\Delta\chi^2(\nu)$  method when the underlying assumptions (*e.g.* Press et al. 1992) are met. Thus, while the  $\Delta\chi^2$  values found in our Monte Carlo simulations do have the same order of magnitude as  $s(\chi^2)$ , it is not clear whether this is significant until more simulations in different modelling contexts have been analyzed.

The experience in dynamical modelling with made-to-measure particle models is still limited, and it is possible that there are some aspects of these methods that influence parameter estimation in different ways than, *e.g.*, Schwarzschild models. However, given the wide-spread use of dynamical modelling for measuring, *e.g.*, dark halo parameters and black hole masses in galaxies, it is important to test the statistical premises of this work more thoroughly. Monte Carlo simulations like those we have performed may be the best way to tackle these issues, and determine the appropriate  $\Delta\chi^2$  values for estimating confidence limits for a given observational and modelling set-up.

### 6.2 Dynamical models for NGC 4494: comparison with the literature

The elliptical galaxy NGC 4494 has previously attracted the attention of several dynamical studies (*e.g.* van der Marel 1991; Kronawitter et al. 2000; Magorrian & Ballantyne 2001; Romanowsky et al. 2003; Rodionov & Athanassoula 2011; Napolitano et al. 2009; Lackner & Ostriker 2010).

Our NMAGIC models improve on the models explored so far in some important aspects. First, we considered as many observational data as currently available, *i.e.* at large radii we had available both PNe velocities (N09) and galaxy spectra in slitlets (F11). The newer slitlets data show a milder drop of the velocity dispersion than what it is suggested by the long-slit data (F11), and this is likely to account for the larger enclosed mass beyond  $\sim 2R_e$  in our results compared to the Jeans models of N09. Second, because of the greater constraining power of the new data compared

to the PNe, we sampled the dark halo parameter space much more finely than before, and for different values of the inclination ( $i = 45^\circ, 70^\circ, 90^\circ$ ). Thirdly, we performed a thorough analysis of the confidence levels at which these parameters can be estimated with our models, given the data at hand. Finally, contrary to most previous studies that considered spherical models (but see Rodionov & Athanassoula 2011), our NMAGIC models are axisymmetric, and we also explored the possibility of flattened dark halos. While the most robust results should eventually be derived using tri-axial models, it has been shown that relaxing the spherical assumption hardly influences the recovered halo mass (see *e.g.* DL09).

Although NGC 4494 was among the three galaxies described as “naked” in Romanowsky et al. (2003), and has an unusually low dark matter fraction in the analysis of Deason et al. (2012), our dynamical models show that a dark matter halo is required. In this respect, they agree with Rodionov & Athanassoula (2011), although the small sequence of explored models did not allow them to put robust constraints on the halo mass, and also with N09. N09 investigated a family of multi-component kurtosis-based Jeans models. Their favoured logarithmic dark halo had  $r_0 = 4R_e$  and  $v_0 = 150 \text{ km s}^{-1}$ . Our best-fitting halo models are more massive than what they obtained (see Section 5), although probably consistent with their errors. These differences are probably mostly due to the additional slitlets constraints that we included, and the better use of the higher-order kinematic moments in the NMAGIC modelling.

The dark matter fraction of our best-fitting NMAGIC models  $f_{\text{DM}}(< 5R_e) = 0.6 \pm 0.1$  is therefore higher than what was reported by N09 (0.2–0.5). Interestingly, the new value agrees very well with the stellar population predictions computed by Deason et al. (2012) assuming a Chabrier initial mass function (see their Fig. 7). Their spherical distribution function models of the PNe velocities, on the other hand, indicated a low dark matter fraction  $f_{\text{DM}}(< 5R_e) = 0.32 \pm 0.12$ .

Alternative estimates of the mass of NGC 4494, *e.g.* from the X-ray emission of hot gas, would be highly desirable. From the compact X-ray gas emission, Fukazawa et al. (2006) estimated  $\Upsilon_B = 6.2 \pm 1.9$  inside  $1R_e$ , consistent with the Jeans modelling of N09 but higher than our NMAGIC results. However, the existence of X-ray emitting gas around this galaxy has been questioned (O’Sullivan & Ponman 2004; Diehl & Statler 2007), and the validity of hydrostatic equilibrium may also be dubious (Ciotti & Pellegrini 1996).

Additional kinematic constraints at large radii could be obtained from different tracers of the mass distribution, such as GCs. However, from the analysis of the spatial and kinematic distributions of blue and red GCs around NGC 4494, which do not follow that of the stars (F11), it is likely that PNe and GCs are in distinct dynamical equilibria in the same gravitational potential (see *e.g.* Das et al. 2011).

Our best-fitting NMAGIC models have a mass-to-light  $\Upsilon_B = 3.71 \pm 0.15$ , obtained converting from  $\Upsilon_V$  using the de-reddened colour from Goudfrooij et al. (1994). This value of the stellar mass-to-light ratio is lower than that obtained from the Jeans models of N09, and is easier to reconcile with independent measurements from stellar population models, which gave  $\Upsilon_B = 4.3 \pm 0.7$  for a Kroupa initial mass function (see N09). In this respect, Lackner & Ostriker (2010) fitted

galaxy formation model to the PNe velocities of NGC 4494, and found that the best-fit dissipational and dissipationless models give  $\Upsilon_B = 2.97$  and  $\Upsilon_B = 3.96$ , respectively, so that a purely dissipational formation scenario for NGC 4494 seemed to be ruled out (Lackner & Ostriker 2010).

Finally, the edge-on NMAGIC models that best reproduce the observational data of NGC 4494 are mildly radially anisotropic, with  $\beta \sim 0.4$  for the 90% confidence range. More inclined NMAGIC models ( $i = 45^\circ$ ) within the same confidence range are more radially anisotropic, *i.e.*  $\beta \sim 0.6$ . The degree of orbital anisotropy is consistent with the previous analysis of N09 and Deason et al. (2012).

### 6.3 The wider context: intermediate-luminosity ellipticals

NGC 4494 belongs to the group of intermediate-luminosity elliptical galaxies with rapidly falling velocity dispersion profile (NGC 821, NGC 3379, NGC 4494, NGC 4697), dubbed “naked” by Romanowsky et al. (2003) because of the unusually low dark matter content revealed by their favoured dynamical models. The analysis of Coccato et al. (2009) identified a larger group of early-type galaxies (NGC 821, NGC 3377, NGC 3379, NGC 4494, NGC 4564, NGC 4697) with strongly decreasing  $v_{\text{rms}} = \sqrt{\sigma^2 + v^2}$  profiles.

Detailed dynamical models have now been obtained for all of the galaxies in the original sample of Romanowsky et al. (2003), including observational constraints from the higher order moments of the LOSVD (see the summary in N09 and Weijmans et al. 2009; Forestell & Gebhardt 2010, for NGC 821). On the whole, the results suggest that these intermediate-luminosity galaxies are inconsistent with the previous claims of little to no dark matter halo.

We now compare the results that we derived for NGC 4494 in this work, with the findings previously obtained by DL08 and DL09 for NGC 4697 and NGC 3379 using the same modelling technique. Indeed, the photometry and kinematics of these three galaxies are not very different. They all have intermediate values of luminosity and stellar mass, similarly low values of the central velocity dispersion  $\sim 150 - 210 \text{ km s}^{-1}$ , and similarly falling  $v_{\text{rms}}$  profiles (Coccato et al. 2009).

Fig. 23 shows the comparison of the NMAGIC models obtained for NGC 4697, NGC 3379, and NGC 4494. For NGC 4494, we plot the range of best-fitting edge-on models as determined in Section 5. For the other intermediate-luminosity ellipticals, no rigorous  $\Delta\chi^2$  analysis was performed, but a range of valid models was determined based on the likelihood of PNe.

As can be seen in the bottom panel of Fig. 23, the orbital structure of the three intermediate luminosity ellipticals is radially biased, in agreement with previous dynamical models of elliptical galaxies in the literature (*e.g.* Merritt & Oh 1997; Rix et al. 1997; Gerhard et al. 1998; van der Marel et al. 1998; Matthias & Gerhard 1999; Gebhardt et al. 2000; Saglia et al. 2000), with predictions of the monolithic collapse scenario (van Albada 1982), and with simulations of both binary-mergers (*e.g.* Gerhard 1981; Dekel et al. 2005; Thomas et al. 2009a) and cosmological mergers (*e.g.* Abadi et al. 2006; Oñorbe et al. 2007), though

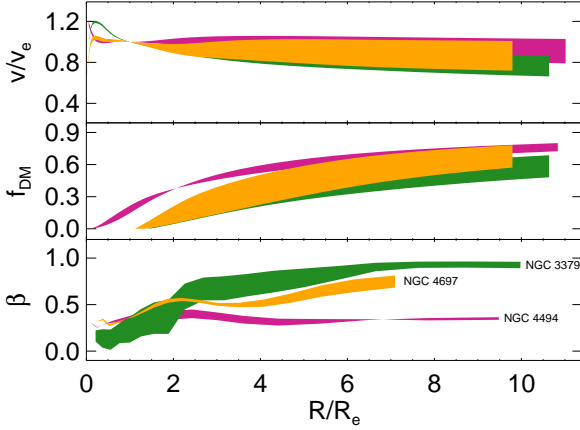


**Figure 23.** From top to bottom: as a function of radius, circular velocity normalized by its value at  $1R_e$ , dark matter fraction, and anisotropy parameter of the range of valid NMAGIC models obtained fitting the data of NGC 4494 (this work, *violet*), NGC 4697 (DL08, *orange*), and NGC 3379 (DL09, *green*).

the remnants of binary mergers can exhibit a variety of orbital distributions (Naab et al. 2006).

NGC 4494 is characterized by a milder level of radial anisotropy than the other two galaxies, consistent with the fact that its projected velocity dispersion is higher (see Fig. 15 of Coccato et al. (2009)) and its surface density profile steeper. Recent simulations have shown that dissipational processes in wet mergers may decrease the level of radial anisotropy (*e.g.* Naab et al. 2006; Thomas et al. 2009b), and also explain many observed features such as counter-rotating disks, kinematically decoupled components, and extra light at small radii (*e.g.* Mihos & Hernquist 1994; Springel et al. 2005; Cox et al. 2006; Jesseit et al. 2007; Hopkins et al. 2008; Hoffman et al. 2010).

All three galaxies have been classified as fast rotators (Emsellem et al. 2011). For NGC 4494, its central kinematically decoupled core (Krajnović et al. 2011), and the small value of  $\lambda_R$  at large radii (Coccato et al. 2009), suggest a complicated rotation structure. Such transitions in  $\lambda_R$  towards large radii (for other cases, see Proctor et al. 2009; Coccato et al. 2009) may be a signature of merger events (*e.g.* Hoffman et al. 2010). The preference for edge-on models found in Section 5.3 also suggests that only a small fraction of the kinetic energy in this galaxy is in rotation.

The top panel of Fig. 23 shows the circular velocity curves normalized at  $1R_e$ . At large radii, the behaviour of the circular velocity is not so different, partially due to the assumption of logarithmic halo profiles. The greatest discrepancies can be seen in the central regions, and are probably due to different imprints left by baryonic processes during galaxy formation.

This is also supported by the fact that the dark matter fractions of these three galaxies are remarkably different (middle panel of Fig. 23), while their global circular velocity curves are more similar. The dark matter fraction of NGC 4494 has much higher values, particularly inside  $3R_e$ , than those of NGC 4697 and NGC 3379. Such a high dark matter fraction could be a consequence of a merger event (like those advocated by Proctor et al. (2009) or F11), which

might have scattered dark matter into the inner regions of the galaxy (Oser et al. 2012; Hilz et al. 2012).

## 7 CONCLUSIONS

We presented dynamical models for the intermediate luminosity elliptical galaxy NGC 4494, fitting photometric and kinematic observational data to investigate its mass distribution and orbital structure. Our extended kinematic data included the recently available integrated light spectra in slitlets (Foster et al. 2011) and hundreds of planetary nebulae velocities reaching out to  $\simeq 7R_e$  (Napolitano et al. 2009). We used the  $\chi^2$ -made-to-measure particle code NMAGIC to construct axisymmetric models for various inclinations exploring a large sequence of gravitational potentials.

In parallel, we carried out a parameter estimation study, investigating how well the characteristic parameters of dark matter halos can be recovered via NMAGIC modelling of the available observational data. For this, we used Monte Carlo simulations of NGC 4494-like mock galaxies to determine the confidence regions around the best-fitting model. These confidence bands were then used to discriminate the range of valid models for NGC 4494.

Our main results can be summarized as follows:

- Given the observational data of NGC 4494 and our NMAGIC modelling set-up, Monte Carlo simulations showed that the usual  $1\sigma$  (70%) confidence level corresponds to a relative difference in the merit function  $\Delta G = 26$  ( $\Delta\chi^2 = 59$ ). At 90% confidence level,  $\Delta G = 32$  and  $\Delta\chi^2 \sim 70$ . These differences are much larger than the commonly used  $\Delta\chi^2$  values based on varying a small number of model parameters.

- Under the assumption that the dark matter halo has a logarithmic parameterization, the best-fitting models for NGC 4494 determined within these confidence levels have an approximately flat total circular velocity curve outside  $\sim 0.5R_e$ , with  $v_c(3R_e) \sim 220\text{kms}^{-1}$ . The larger variation is in the dark matter circular velocity curve, rather than in the stellar one. The dark matter fraction of the models within 70% confidence level is about  $0.6 \pm 0.1$  at  $5R_e$ , and they are embedded in concentrated dark halos ( $r_0 \sim 1-2R_e$ ) with circular velocity  $\sim [160-230]\text{kms}^{-1}$ . With this large dark matter fraction, the stellar mass-to-light ratio is consistent with the value predicted by Deason et al. (2012) from stellar population models with a Chabrier IMF. The discrepancy with the more diffuse halo found by the Jeans models of Napolitano et al. (2009) is likely due to the additional slitlets constraints, which suggest a milder drop of the velocity dispersion than shown by the long-slit kinematics.

- The edge-on models provide the best fits to the available observational data, but the inferred dark halo parameters ( $r_0, v_0$ ) do not depend sensitively on the assumed inclination. We explored a sequence of flattened dark matter halos, which however did not change our main result: edge-on models provide better fits to the data than models with lower inclinations.

- The orbital anisotropy of the stars is increasingly radial from the center outwards, but the amount of radial anisotropy is smaller than what was found in similar previous works for the two other intermediate luminosity elliptical

cals with rapidly falling, quasi-Keplerian velocity dispersion profiles, NGC 3379 and NGC 4697.

- Comparing the halos of all three intermediate-luminosity, quasi-Keplerian ellipticals modelled with the same made-to-measure particle technique (NGC 3379, NGC 4697 and NGC 4494), we conclude that they have similar global circular velocity curves and outer dark matter halos. NGC 4494 shows a particularly high dark matter fraction inside  $\sim 3R_e$ , and a strong central concentration of baryons. These differences are probably related to the detailed interplay between baryons and dark matter in the processes which shaped these galaxies.

## ACKNOWLEDGEMENTS

The authors thank Caroline Foster and Duncan Forbes for providing the slitlets data before publication, Nicola Napolitano for useful discussions, and an anonymous referee for a careful reading of the paper. LM acknowledges support from and participation in the International Max-Planck Research School on Astrophysics at the Ludwig-Maximilians University. LC acknowledges financial support from the European Community's Seventh Framework Programme (/FP7/2007-2013/) under grant agreement No. 229517. IMV acknowledges support from the DFG Priority Program SPP 1177.

## REFERENCES

- Abadi M. G., Navarro J. F., Steinmetz M., 2006, *MNRAS*, 365, 747
- Adams J. J., Gebhardt K., Blanc G. A., Fabricius M. H., Hill G. J., Murphy J. D., van den Bosch R. C. E., van de Ven G., 2012, *ApJ*, 745, 92
- Auger M. W., Treu T., Bolton A. S., Gavazzi R., Koopmans L. V. E., Marshall P. J., Moustakas L. A., Burles S., 2010, *ApJ*, 724, 511
- Barth A. J., Sarzi M., Rix H.-W., Ho L. C., Filippenko A. V., Sargent W. L. W., 2001, *ApJ*, 555, 685
- Bender R., Saglia R. P., Gerhard O. E., 1994, *MNRAS*, 269, 785
- Bertola F., Pizzella A., Persic M., Salucci P., 1993, *ApJ*, 416, L45
- Binney J., Mamon G. A., 1982, *MNRAS*, 200, 361
- Binney J., Tremaine S., 2008, *Galactic Dynamics: Second Edition*, Binney, J. & Tremaine, S., ed. Princeton University Press
- Bissantz N., Debattista V. P., Gerhard O., 2004, *ApJ*, 601, L155
- Cappellari M., Neumayer N., Reunanen J., van der Werf P. P., de Zeeuw P. T., Rix H.-W., 2009, *MNRAS*, 394, 660
- Cappellari M., Verolme E. K., van der Marel R. P., Kleijn G. A. V., Illingworth G. D., Franx M., Carollo C. M., de Zeeuw P. T., 2002, *ApJ*, 578, 787
- Chanamé J., Kleyna J., van der Marel R., 2008, *ApJ*, 682, 841
- Ciotti L., Morganti L., de Zeeuw P. T., 2009, *MNRAS*, 393, 491
- Ciotti L., Pellegrini S., 1996, *MNRAS*, 279, 240
- Coccato L. et al., 2009, *MNRAS*, 394, 1249
- Cox T. J., Dutta S. N., Di Matteo T., Hernquist L., Hopkins P. F., Robertson B., Springel V., 2006, *ApJ*, 650, 791
- Cretton N., Rix H.-W., de Zeeuw P. T., 2000, *ApJ*, 536, 319
- Cretton N., van den Bosch F. C., 1999, *ApJ*, 514, 704
- Das P., Gerhard O., Churazov E., Zhuravleva I., 2010a, *MNRAS*, 409, 1362
- Das P., Gerhard O., Churazov E., Zhuravleva I., 2010b, *MNRAS*, 409, 1362
- Das P., Gerhard O., Mendez R. H., Teodorescu A. M., de Lorenzi F., 2011, *MNRAS*, 415, 1244
- de Lorenzi F., Debattista V. P., Gerhard O., Sambhus N., 2007, *MNRAS*, 376, 71
- de Lorenzi F. et al., 2009, *MNRAS*, 395, 76
- de Lorenzi F., Gerhard O., Saglia R. P., Sambhus N., Debattista V. P., Pannella M., Méndez R. H., 2008, *MNRAS*, 385, 1729
- de Vaucouleurs G., de Vaucouleurs A., Corwin, Jr. H. G., Buta R. J., Paturel G., Fouque P., 1991, *Sky & Telescope*, 82, 621
- Deason A. J., Belokurov V., Evans N. W., McCarthy I. G., 2012, *ApJ*, 748, 2
- Debattista V. P., Sellwood J. A., 2000, *ApJ*, 543, 704
- Dehnen W., 2009, *MNRAS*, 395, 1079
- Dehnen W., Gerhard O. E., 1993, *MNRAS*, 261, 311
- Dekel A., Stoehr F., Mamon G. A., Cox T. J., Novak G. S., Primack J. R., 2005, *Nature*, 437, 707
- Diehl S., Statler T. S., 2007, *ApJ*, 668, 150
- Douglas N. G. et al., 2002, *PASP*, 114, 1234
- Emsellem E. et al., 2011, *MNRAS*, 414, 888
- Fall S. M., Efsthathiou G., 1980, *MNRAS*, 193, 189
- Forbes D. A., Franx M., Illingworth G. D., 1995, *AJ*, 109, 1988
- Forbes D. A., Franx M., Illingworth G. D., Carollo C. M., 1996, *ApJ*, 467, 126
- Forestell A. D., Gebhardt K., 2010, *ApJ*, 716, 370
- Foster C. et al., 2011, *MNRAS*, 906
- Franx M., van Gorkom J. H., de Zeeuw T., 1994, *ApJ*, 436, 642
- Fukazawa Y., Botoya-Nonesca J. G., Pu J., Ohto A., Kawano N., 2006, *ApJ*, 636, 698
- Gebhardt K. et al., 2003, *ApJ*, 597, 239
- Gebhardt K. et al., 2000, *AJ*, 119, 1157
- Gerhard O., Jeske G., Saglia R. P., Bender R., 1998, *MNRAS*, 295, 197
- Gerhard O. E., 1981, *MNRAS*, 197, 179
- Gerhard O. E., 1991, *MNRAS*, 250, 812
- Gerhard O. E., 1993, *MNRAS*, 265, 213
- Gerhard O. E., Binney J. J., 1996, *MNRAS*, 279, 993
- Goudfrooij P., de Jong T., Hansen L., Norgaard-Nielsen H. U., 1994, *MNRAS*, 271, 833
- Hilz M., Naab T., Ostriker J. P., Thomas J., Burkert A., Jesseit R., 2012, *ArXiv e-prints*
- Hoffman L., Cox T. J., Dutta S., Hernquist L., 2010, *ApJ*, 723, 818
- Hopkins P. F., Hernquist L., Cox T. J., Dutta S. N., Rothberg B., 2008, *ApJ*, 679, 156
- Hui X., Ford H. C., Freeman K. C., Dopita M. A., 1995, *ApJ*, 449, 592
- Humphrey P. J., Buote D. A., Gastaldello F., Zappacosta L., Bullock J. S., Brighenti F., Mathews W. G., 2006, *ApJ*, 646, 899

- Jesseit R., Naab T., Peletier R. F., Burkert A., 2007, *MNRAS*, 376, 997
- Kalnajs A. J., 1977, *ApJ*, 212, 637
- Keeton C. R., 2001, *ApJ*, 561, 46
- Krajinović D. et al., 2011, *MNRAS*, 414, 2923
- Kronawitter A., Saglia R. P., Gerhard O., Bender R., 2000, *A&AS*, 144, 53
- Lackner C. N., Ostriker J. P., 2010, *ApJ*, 712, 88
- Lauer T. R. et al., 2005, *AJ*, 129, 2138
- Loewenstein M., White, III R. E., 1999, *ApJ*, 518, 50
- Long R. J., Mao S., 2010, *MNRAS*, 405, 301
- Long R. J., Mao S., 2012, *MNRAS*, 421, 2580
- Long R. J., Mao S., Shen J., Wang Y., 2013, *MNRAS*, 428, 3478
- Magorrian J., 1999, *MNRAS*, 302, 530
- Magorrian J., Ballantyne D., 2001, *MNRAS*, 322, 702
- Maoz D., Rix H.-W., 1993, *ApJ*, 416, 425
- Matthias M., Gerhard O., 1999, *MNRAS*, 310, 879
- Méndez R. H., Riffeser A., Kudritzki R.-P., Matthias M., Freeman K. C., Arnaboldi M., Capaccioli M., Gerhard O. E., 2001, *ApJ*, 563, 135
- Merrett H. R. et al., 2003, *MNRAS*, 346, L62
- Merritt D., Oh S. P., 1997, *AJ*, 113, 1279
- Mihos J. C., Hernquist L., 1994, *ApJ*, 437, L47
- Morganti L., Gerhard O., 2012, *MNRAS*, 422, 1571
- Murphy J. D., Gebhardt K., Adams J. J., 2011, *ApJ*, 729, 129
- Naab T., Jesseit R., Burkert A., 2006, *MNRAS*, 372, 839
- Napolitano N. R. et al., 2011, *MNRAS*, 411, 2035
- Napolitano N. R. et al., 2009, *MNRAS*, 393, 329
- Oñorbe J., Domínguez-Tenreiro R., Sáiz A., Serna A., 2007, *MNRAS*, 376, 39
- Oosterloo T. A., Morganti R., Sadler E. M., Vergani D., Caldwell N., 2002, *AJ*, 123, 729
- Oser L., Naab T., Ostriker J. P., Johansson P. H., 2012, *ApJ*, 744, 63
- O'Sullivan E., Ponman T. J., 2004, *MNRAS*, 349, 535
- Peng E. W., Ford H. C., Freeman K. C., 2004, *ApJ*, 602, 705
- Persic M., Salucci P., Stel F., 1996, *MNRAS*, 281, 27
- Press W. H., Teukolsky S. A., Vetterling W. T., Flannery B. P., 1992, *Numerical recipes in FORTRAN. The art of scientific computing*, Press, W. H., Teukolsky, S. A., Vetterling, W. T., & Flannery, B. P., ed.
- Proctor R. N., Forbes D. A., Romanowsky A. J., Brodie J. P., Strader J., Spolaor M., Mendel J. T., Spitler L., 2009, *MNRAS*, 398, 91
- Rix H.-W., de Zeeuw P. T., Cretton N., van der Marel R. P., Carollo C. M., 1997, *ApJ*, 488, 702
- Rodionov S. A., Athanassoula E., 2011, *MNRAS*, 410, 111
- Romanowsky A. J., Douglas N. G., Arnaboldi M., Kuijken K., Merrifield M. R., Napolitano N. R., Capaccioli M., Freeman K. C., 2003, *Science*, 301, 1696
- Saglia R. P., Kronawitter A., Gerhard O., Bender R., 2000, *AJ*, 119, 153
- Sellwood J. A., 2003, *ApJ*, 587, 638
- Shapiro K. L., Cappellari M., de Zeeuw T., McDermid R. M., Gebhardt K., van den Bosch R. C. E., Statler T. S., 2006, *MNRAS*, 370, 559
- Springel V., Di Matteo T., Hernquist L., 2005, *MNRAS*, 361, 776
- Syer D., Tremaine S., 1996, *MNRAS*, 282, 223
- Thomas J., Jesseit R., Naab T., Saglia R. P., Burkert A., Bender R., 2007a, *MNRAS*, 381, 1672
- Thomas J. et al., 2009a, *MNRAS*, 393, 641
- Thomas J., Saglia R. P., Bender R., Thomas D., Gebhardt K., Magorrian J., Corsini E. M., Wegner G., 2005, *MNRAS*, 360, 1355
- Thomas J., Saglia R. P., Bender R., Thomas D., Gebhardt K., Magorrian J., Corsini E. M., Wegner G., 2007b, *MNRAS*, 382, 657
- Thomas J., Saglia R. P., Bender R., Thomas D., Gebhardt K., Magorrian J., Corsini E. M., Wegner G., 2009b, *ApJ*, 691, 770
- Tonry J. L., Dressler A., Blakeslee J. P., Ajhar E. A., Fletcher A. B., Luppino G. A., Metzger M. R., Moore C. B., 2001, *ApJ*, 546, 681
- Treu T., Koopmans L. V. E., 2004, *ApJ*, 611, 739
- Valluri M., Merritt D., Emsellem E., 2004, *ApJ*, 602, 66
- van Albada T. S., 1982, *MNRAS*, 201, 939
- van den Bosch R. C. E., de Zeeuw P. T., 2010, *MNRAS*, 401, 1770
- van den Bosch R. C. E., van de Ven G., 2009, *MNRAS*, 398, 1117
- van der Marel R. P., 1991, *MNRAS*, 253, 710
- van der Marel R. P., Cretton N., de Zeeuw P. T., Rix H., 1998, *ApJ*, 493, 613
- van der Marel R. P., Magorrian J., Carlberg R. G., Yee H. K. C., Ellingson E., 2000, *AJ*, 119, 2038
- Verolme E. K. et al., 2002, *MNRAS*, 335, 517
- Weijmans A.-M. et al., 2009, *MNRAS*, 398, 561